RESEARCH ARTICLE | JANUARY 23 2026

Contact network structures and rigidity development in two-dimensional bidisperse suspensions

Rahul Pandare ; Michel Orsi ; Mark D. Shattuck ; Bulbul Chakraborty ; Jeffrey F. Morris

J. Rheol. 70, 343–359 (2026)
https://doi.org/10.1122/8.0001127

Contact network structures and rigidity development in two-dimensional bidisperse suspensions

Rahul Pandare,[1,2] Michel Orsi,[1,3] Mark D. Shattuck,[1,4] Bulbul Chakraborty,[5] and Jeffrey F. Morris[1,2,a)]

[1]*Benjamin Levich Institute, CUNY City College of New York, New York, New York 10031*
[2]*Department of Chemical Engineering, CUNY City College of New York, New York, New York 10031*
[3]*Politecnico di Torino, Corso Duca degli Abruzzi 24, 10129 Torino, Italy*
[4]*Department of Physics, CUNY City College of New York, New York, New York 10031*
[5]*Martin Fisher School of Physics, Brandeis University, Waltham, Massachusetts 02454*

(Received 23 September 2025; final revision received 11 December 2025; published 23 January 2026)

Abstract

Dense non-Brownian suspensions with conservative repulsive forces between the particles are known to exhibit shear thickening, where viscosity increases with applied stress due to a change in the dominant stress mechanism. At low stress, repulsion maintains liquid films that lubricate particle interactions, while higher stress overcomes the repulsion to generate frictional contacts and leads to greater flow resistance. Here, shear-thickened suspensions are studied in stress-controlled simulations incorporating hydrodynamic, electrostatic double-layer repulsion, and frictional forces; two-dimensional monolayers are studied for monodisperse and bidisperse suspensions with size ratios $\delta = a_s/a_l$ from 1.0 to 4.0, where a_s and a_l are the small and large particle radii. Small-particle fractions $\zeta = \phi_s/\phi = 0.25$, 0.50, and 0.75 are considered. Total area fractions of $0.71 \leq \phi \leq 0.82$ are studied, with the larger values at greater size ratios. Flow curves for mono- and bidisperse systems under varying stress are analyzed, along with detailed structural comparisons for different interparticle friction. We examine the approach to shear jamming, through the emergence of rigid local clusters generated by the reduction of degrees of freedom by frictional contacts. The variance of the fraction of particles in rigid clusters increases sharply near the jamming solid fraction, consistent with a second-order phase transition description of the phenomenon. The contact fabric tensor is determined to provide a measure of the structural anisotropy. https://doi.org/10.1122/8.0001127

I. INTRODUCTION

The flow of dense suspensions is encountered in a variety of industrial and natural processes. These include the manufacturing of cement [1,2], pastes [3,4], and chocolate [5,6], as well as geophysical events, such as mudflows [7], landslides [8], and lava flows [9,10]. Understanding the rheological behavior of dense suspensions is crucial for accurate prediction of their mechanical response in these natural and applied environments.

Suspensions of solid particles in a Newtonian fluid frequently exhibit non-Newtonian behavior, and very strong shear thickening and shear jamming have been shown to be related to a transition from lubricated to frictional interactions [11,12]. In the present study, we focus on dense frictional suspensions with an emphasis on bidisperse systems. A monolayer, or two-dimensional, system is studied as this allows use of established algorithms for the evaluation of local structures that have recently been related to the approach to jamming [13,14].

Related work on bidisperse suspensions of frictional particles has been performed. Pednekar *et al.* [15] examined polydisperse systems and their rheological equivalents in bidisperse formulations, for stresses above the shear-thickening transition where the response was rate-independent. Malbranche *et al.* [16] extended this work by simulating the rate-dependent rheology of bidisperse suspensions, across varying size ratios and volume fractions, demonstrating that the Maron–Pierce power-law relation [17] effectively captures the influence of these parameters. A key outcome of these studies is that if the maximum packing fraction, denoted $\phi_m(\sigma)$ in this work to indicate its stress-dependence, is known, then an empirical viscosity model (e.g., Maron–Pierce) can provide good descriptions of the stress response. However, these studies did not probe this fitting very close to jamming. Here, our focus is on study of the regime near the maximum packing fraction and the transition from flowing to shear jamming, seeking to deduce the defining characteristics of the events leading to this transition. Particular emphasis is placed on probing the microstructural origins of shear jamming, which are shown here—by extension of related prior work [13,14]—to result from the development and percolation of rigid clusters induced by stress-induced frictional contact. Additionally, we analyze and quantify for the first time in a dense suspension flow the contact network fabric and show how this depends on the solid fraction for varying bidispersity parameters.

Dense suspensions under shear exhibit shear thinning [18,19] as well as the noted shear thickening [20,21] and shear jamming [22,23]. Shear thinning or thickening implies a decrease or increase of the apparent viscosity with shear rate, while shear jamming implies that a material is driven from a flowing state to a jammed solid by imposed stress. In the concentrated suspensions of interest here, both

a)Author to whom correspondence should be addressed; electronic mail: morris@ccny.cuny.edu

discontinuous shear thickening (DST) and continuous shear thickening (CST) may occur. DST is characterized by an onset solid fraction at which $\partial\eta/\partial\dot{\gamma} \to \infty$, with larger ϕ showing stress (or viscosity) discontinuity when presented as a function of the shear rate $\dot{\gamma}$. CST corresponds to a more gradual increase in viscosity with increasing shear rate. Shear jamming is encountered at sufficiently large stress when $\phi \geq \phi_m^\mu$ (often denoted ϕ_J^μ), which represents the jamming solid fraction at asymptotically large stress, i.e., for stresses large enough to overcome any repulsive interactions [22,24,25]. Here, μ represents the interparticle friction coefficient and indicates that ϕ_m depends on μ, generally decreasing as μ increases. We will denote the maximum flowable packing fraction at lower stress as $\phi_m(\sigma)$, omitting the μ dependence, to show that the material may exhibit a different maximum flowable fraction as stress increases, as shown for dense bidisperse suspensions in Malbranche *et al.* [16].

The current work does not address the shear-thickening behavior, but instead describes an investigation of the rheology of two-dimensional (2D) dense bidisperse suspensions, for stresses above those resulting in thickening. The study covers a range of area fraction range $0.71 \leq \phi \leq 0.82$, and several values of both the size ratio $\delta = a_l/a_s$ and the small-particle area fraction $\zeta = \phi_s/\phi$. The spherical particle radii are a_s and a_l for the large and small particles, respectively, while ϕ_s is the area fraction occupied by the small particles alone. Note that in this work, ϕ denotes the area fraction since we consider a monolayer of spheres. The general phenomenology of dense 2D suspensions [14] agrees with that of 3D suspensions (where ϕ would be the volume fraction) [15,16,26]. To simulate the suspension flow, we employ the Lubricated-Flow Discrete Element Method (LF-DEM) [12,27]. The LF-DEM has proven to be successful in capturing key rheological features of dense suspensions, such as DST, CST, and shear thinning; LF-DEM is detailed in Sec. II A. This study investigates the microstructural evolution of dense suspensions under shear, with a focus on shear jamming and stress-induced structural transitions. We analyze contact pair distributions, flow-curve stress responses, and anisotropy, the latter characterized for systems with both infinite and finite friction coefficients.

Recalling that $F_{C,\tan}/F_{C,nor} < \mu$ for nonsliding interactions at contact between particles ($F_{C,\tan}$ is the tangential and $F_{C,nor}$ is the normal force between the pair), considering an infinite-friction coefficient provides a limiting case in which any compressive contact normal force between two particles couples the rotational degrees of freedom of the pair. This coupling is important because in dense suspensions subjected to high shear stress, simulations show that particles are driven into transient structures or "clusters" with reduced degrees of freedom [13,14], and these structures are essential to the observed viscosity increase; here, the approach to jamming is probed and is distinct from a recent work by Goyal *et al.* [28] that probed the onset of DST and the role of percolation of structures satisfying the local isostatic condition. The clusters we consider consist of frictionally interacting particles with highly correlated motion, and for sufficiently reduced degrees of freedom, the clusters may exhibit locally rigid motion. To characterize and quantify the onset of rigidity, constraint-counting methods, such as Maxwell's rigidity criterion, provide a fundamental framework [29]. Originally developed for the mechanical stability of trusses, Maxwell's constraint-counting method establishes a criterion for mechanical rigidity based on the number of available degrees of freedom (DOF) in the system. For N particles in a d-dimensional space, the total DOF can be expressed as

$$\mathrm{DOF} = N\left[d + \frac{1}{2}d(d-1)\right] = \frac{N}{2}d(d+1). \tag{1}$$

For a 2D system, where each particle possesses two translational and one rotational degree of freedom, $\mathrm{DOF} = 3N$. When the number of constraints is sufficient to fully restrict these degrees of freedom (constraints $\geq 3N$), the suspension exhibits bulk rigidity: it is in a mechanically stable state where the network of particle contacts resists deformation under applied stress. However, this is a mean-field approximation and thus only provides a global condition for rigidity and does not account for the spatial heterogeneity in contact networks. In dense suspensions, local mesoscale structural networks play a critical role in the material's response to stress [14,30]. The formation of local rigid clusters and their percolation across the system requires a more involved approach, for which we turn to the *pebble game* (PG) algorithm, which is described in Sec. II B.

Shear jamming in athermal granular particulate systems, where there is a transition from a flowing state to a shear-jammed solid, has been extensively studied [31,32]. Bi *et al.* demonstrated shear jamming in granular disks at a fixed volume setup [33]. However, the transition to shear jamming in dense suspensions has not been fully explored. Recent studies have highlighted that isostatic jammed packings for granular materials occur at a specific average shear strain $\langle\gamma\rangle$ from an unjammed initial state [34]. In general, the nature of the jamming transition is governed by particle interactions, applied shear stress, and the interparticle friction coefficient [23,33]. For both industrial suspensions, such as those in ceramic precursors [35] or foodstuffs [36], naturally occurring suspensions, such as muds [37], and the jamming characteristics also depend on the size dispersity of the mixture [38,39]. This requires consideration of the size ratio, δ, and the small-particle fraction, ζ. Although these systems are technically polydisperse, they are sometimes dominated by two distinct particle sizes, making them effectively bidisperse. In some muds, ζ can govern critical behaviors, such as landslide initiation [37]. The ratio of large to small particle sizes can be substantial—for example, $\delta > 10$ occurs in soils containing both sand and clay [37], in pharmaceutical products where excipients are mixed with active pharmaceutical ingredients (APIs) [40–42], and in chocolate processing where cocoa particles are blended with much larger sugar crystals [43]. While we do not explore such extreme size ratios, the largest value we consider, $\delta = 4$, does show behavior that is distinct from the lower-δ cases. In addition to the noted dependence on size ratio, we also characterize the dependence based on the small-particle fraction ζ.

A novelty of this work is, thus, that it addresses the structural characteristics near and at jamming of bidisperse suspensions, and relates this behavior to the rheology at a lower solid fraction. The key findings of the work are related to the influence of strong fluctuations of the size and prevalence of rigid clusters at a critical solid fraction in determining the actual jamming fraction.

In Sec. II, we describe the methods employed, followed by results in Sec. III, and conclusions from the work in Sec. IV.

II. METHOD AND SIMULATIONS

A. Model

We perform stress-controlled simulations of a monolayer of spheres, constrained to move in a single plane. This two-dimensional flow is studied for monodisperse and bidisperse spheres using LF-DEM [12]. The LF-DEM model employed considers only short-range particle interactions and solves the overdamped Langevin equations governing particle motion. We include the influence of hydrodynamic $\mathbf{F}_{\mathrm{H}}$, electrical double layer (EDL) repulsion $\mathbf{F}_{\mathrm{R}}$, and contact forces $\mathbf{F}_{\mathrm{C}}$ (as well as torques), all of which are balanced to describe the behavior of the suspension under shear,

$$\mathbf{F}_{\mathrm{H}}(\mathbf{x}, \mathbf{U}_{\mathrm{p}}) + \mathbf{F}_{\mathrm{R}}(\mathbf{x}) + \mathbf{F}_{\mathrm{C}}(\mathbf{x}, \mathbf{U}_{\mathrm{p}}) = 0, \tag{2}$$

where the hydrodynamic force is given by

$$\mathbf{F}_{\mathrm{H}} = -\mathscr{R}_{\mathrm{FU}} \cdot (\mathbf{U}_{\mathrm{p}} - \mathbf{U}_{\infty}) + \mathscr{R}_{\mathrm{FE}} : \mathbf{E}_{\infty}. \tag{3}$$

Here, $\mathbf{U}_{\mathrm{p}}$ is the particle velocity and $\mathbf{U}_{\infty}$ is the imposed shear flow velocity. The strain rate tensor is denoted by $\mathbf{E}_{\infty}$. We consider simple shear flow, for which the relevant components of the strain rate tensor are $\mathrm{E}_{\infty}^{12} = \mathrm{E}_{\infty}^{21} = \dot{\gamma}/2$, where $\dot{\gamma}$ is the imposed shear rate. Here, 1 and 2 denote the flow and velocity gradient directions, respectively. The translational-rotational resistance matrix is given by

$$\mathscr{R}_{\mathrm{FU}} = \mathscr{R}_{\mathrm{Stokes}} + \mathscr{R}_{\mathrm{Lubrication}}, \tag{4}$$

where $\mathscr{R}_{\mathrm{Stokes}}$ is a diagonal matrix that gives the (single-body) Stokes drag force and torque for each particle and $\mathscr{R}_{\mathrm{Lubrication}}$ and $\mathscr{R}_{\mathrm{FE}}$ are sparse resistance matrices that give the two-body lubrication forces (and torques) and drag, respectively, and are functions of particle positions [44,45]. Repulsion in the form of an EDL is introduced for interacting particle and is given by [46]

$$\mathbf{F}_{\mathrm{R}} = \begin{cases} \mathbf{F}_0 \cdot \mathrm{D}^* \cdot \exp(-d/\lambda) & \text{if } d \geq 0, \\ \mathbf{F}_0 \cdot \mathrm{D}^* & \text{if } d < 0, \end{cases} \tag{5}$$

where

$$\mathrm{D}^* = \frac{2a_i a_j}{a_s(a_i + a_j)}, \quad d = r - a_i - a_j. \tag{6}$$

Here, D^* is a geometric factor that scales the EDL repulsion according to particle size asymmetry. $\mathbf{F}_0$ is the repulsive force that acts along the line of centers, $\mathbf{r}_{ij} = \mathbf{r}_i - \mathbf{r}_j$, of the two interacting particles i and j. D^* denotes the normalized effective diameter of the interacting particle pair, where a_i and a_j are the radii of the two interacting particles. The minimum separation distance between their surfaces is given by d, with $r = |\mathbf{r}_i - \mathbf{r}_j|$ being the center-to-center distance. The radius of the smaller particle a_s serves as a characteristic length scale for normalization. The Debye length, λ, defines the characteristic distance over which the EDL repulsion decays and depends on the ionic strength and dielectric properties of the solvent. In this work, we set $\lambda = 0.05a_s$ to represent the strongly screened, short-ranged DLVO (Derjaguin-Landau-Verwey-Overbeek) repulsion typical of dense colloidal suspensions at high ionic strength [47,48]. This choice is also consistent with previous studies on similar systems [12,14,16].

Obtaining shear-rate dependent rheology for hard spheres in non-Brownian suspensions is not straightforward. The lubrication hydrodynamic forces lack a natural force scale for comparison. Once this lubrication film ruptures and hard particle contacts are established, the resulting contact forces can, in principle, support arbitrarily large loads. To establish a meaningful comparison with hydrodynamic forces, an additional force scale is required. This is provided by the repulsive force, $\mathbf{F}_0$, which is, thus, the basis for the emergence of shear-rate dependent rheology in the system studied here. The characteristic shear rate is then defined as $\dot{\gamma}_0 = F_0/6\pi\eta_0 a_s^2$, where $F_0 = |\mathbf{F}_0|$, and the corresponding stress scale is $\sigma_0 = F_0/6\pi a_s^2$, where η_0 is the viscosity of the suspending fluid. We perform most of the simulations in this study at large imposed stress of $\sigma = 100\sigma_0$, except for those cases used to develop flow curves to illustrate the rate dependence for the various bidisperse mixtures (see Fig. 10).

To model frictional contacts, the LF-DEM model employs the stick/slide contact approach, incorporating springs and dashpots (Cundall–Strack model) [49],

$$F_{\mathrm{C,nor}} = k_n h + k_n' U_n, \tag{7}$$

$$F_{\mathrm{C,tan}} = k_t \xi, \tag{8}$$

$$\mathbf{T}_{\mathrm{C}} = \mathbf{a}_i \times \mathbf{F}_{\mathrm{C,tan}}. \tag{9}$$

Here, k_n and k_t are normal and tangential spring constants, respectively, and k_n' is the damping constant, U_n is the normal component of the pair relative velocity, ξ is the tangential spring stretch, and h is the nondimensional interparticle gap, $h = 2d/(a_i + a_j)$. For nonsliding frictional contacts, the interaction force satisfies the Coulomb friction law $F_{\mathrm{C,tan}} \leq \mu F_{\mathrm{C,nor}}$, where μ is the coefficient of friction. We perform stress-controlled simulations, wherein the shear rate and particle velocity are computed for each time step as

$$\dot{\gamma} = \frac{\sigma - \sigma_r - \sigma_c}{\eta_0(1 + 2.5\phi) + \eta_h}, \tag{10}$$

$$\eta_h = V^{-1}\left\{\left(\mathscr{R}_{\mathrm{SE}} - \mathscr{R}_{\mathrm{SU}} \cdot \mathscr{R}_{\mathrm{FU}}^{-1} \cdot \mathscr{R}_{\mathrm{FE}}\right) : \mathbf{E}_{\infty}\right\}_{12}, \tag{11}$$

$$\mathbf{U}_P = \mathbf{U}_\infty + \mathscr{R}_{FU}^{-1} \cdot (\mathscr{R}_{FE} : \mathbf{E}_\infty + \mathbf{F}_R + \mathbf{F}_C). \quad (12)$$

The fluid contribution to the suspension viscosity is given by the denominator of Eq. (10)—$\eta_0(1 + 2.5\phi) + \eta_h$, where η_h is the hydrodynamic interaction portion. $\mathscr{R}_{SE}$ and $\mathscr{R}_{SU}$ are resistance matrices, which give the lubrication stress from the particle velocity and resistance to deformation [45], respectively, and V is the area of the simulation unit cell. The model employs periodic boundary conditions in the direction of the flow and Lees–Edwards [50] periodic boundary conditions in the velocity gradient direction.

LF-DEM has been widely employed to investigate the rheology of dense suspensions. A few points to note about the simulational model are: (i) The particles are suspended in a density-matched fluid, so that there are no buoyancy effects. (ii) External forces, such as gravity, are not considered. (iii) The suspension is non-Brownian; i.e., $Pe = 6\pi\eta_0 a^3\dot{\gamma}/k_B T \to \infty$. (iv) The motion is inertialess; i.e., $Re = \rho\dot{\gamma}a^2/\eta_0 \to 0$.

B. Pebble game

The PG algorithm, developed by Jacobs and Thorpe [51] and later adapted for frictional particle systems by Henkes *et al.* [52], provides a graph-theoretic approach that decomposes the contact network into rigid and floppy subgraphs, allowing identification of locally rigid structures.

The PG as used here to identify rigid clusters within the suspension's contact network can be broken down into four steps: (i) The LF-DEM simulation identifies the frictional and sliding contacts between the interacting pairs. In the PG, each particle is represented as a node, and each contact is represented as an edge or bond in the graph. Frictional contacts impose two constraints, so they are assigned two bonds, whereas sliding contacts impose only one constraint and are assigned a single bond. (ii) Next, the algorithm initializes each node with pebbles corresponding to its DOF. Since the system is two-dimensional, each particle has three DOF (two translational and one rotational), and so each node starts with three pebbles. (iii) The algorithm then covers bonds with pebbles, moving these from the particle center to the bond. A bond can have a maximum of one pebble. A bond that accommodates a pebble is considered a necessary constraint, whereas any bond that remains unoccupied by pebbles is deemed redundant. The number of remaining pebbles per node after redistribution provides the available DOF at each particle. (iv) Finally, rigid clusters are identified by locating the largest subgraphs where the number of leftover pebbles is three or fewer, as three DOF is the maximum allowable for a rigid structure in two dimensions. A system-spanning rigid cluster indicates that the suspension has transitioned into a mechanically stable state. Note, however, that the slight deformability of our particles (and greater deformability in prior studies of suspensions using the PG algorithm [13,14]) is not accounted and may allow motion to continue despite the satisfaction of this condition for global rigidity.

Unlike Maxwell's mean-field approach, which assumes homogeneity, the PG captures the spatially heterogeneous distribution of constraints, revealing localized rigid clusters. This rigidity metric considers only frictional constraints, neglecting repulsive and hydrodynamic forces that can destabilize clusters and enable viscous flow, so the resulting structures are termed "minimally rigid" [13]. The PG algorithm is currently defined only for two-dimensional networks, which motivated our focus on a 2D suspension in this study. At present, no established analog of the pebble game exists for three-dimensional systems.

C. Suspensions

The 2D simulations in this study consider $N = 1000$ frictional particles. For monodisperse suspensions, ϕ (area fraction here and volume fraction in 3D) is used as the primary characterization parameter. However, for bidisperse suspensions, additional parameters are required. The ratio of the radii of large a_l to small a_s particles is given by

$$\delta = \frac{a_l}{a_s}. \quad (13)$$

The area ratio is the fraction of the total solid area occupied by small particles,

$$\zeta = \frac{\phi_s}{\phi}. \quad (14)$$

Simulations are performed in the dense regime, at area fractions in the range $0.71 \le \phi \le 0.82$. The size ratios studied span from monodisperse ($\delta = 1.0$) up to $\delta = 4.0$, with intermediate values $\delta = 1.4$ and $\delta = 2.0$. Figures 1(a)–1(c) illustrate variations in bidispersity at fixed ϕ and ζ, while (d)–(f) show variations in ζ at fixed ϕ and δ.

We present three sets of simulations. (i) Results presented in Secs. III A–III D are obtained from systems at the limit of very large friction; we consider the coefficient of friction to be infinite and denote it as $\mu \to \infty$ to describe these simulations. In this limit, all contacting particles interact through fully frictional, nonsliding contacts, for any finite compressive normal force between the pair. The fractions of small particles studied are $\zeta = 0.25$, 0.50, and 0.75. As noted, the simulations are stress-controlled, at $\sigma = 100\sigma_0$. We choose a large shear stress in order to allow a focus on the shear-jamming transition as a function of ϕ; the flow-state diagram in Fig. 2 is helpful in seeing the part of parameter space in which the work occurs. Each run proceeds to a cumulative strain of $\gamma = 20$, with two independent replicates per condition. In this section, we focus on rheology and contact structures close to and at the shear-jamming condition, presenting most of the results discussed in this work. (ii) Section III E reports flow-curve data for $\mu \to \infty$. A small-particle area fraction is fixed at $\zeta = 0.50$. However, the simulations are performed at different size ratios, δ, with solid fractions chosen such that the cases at different δ are comparably distant from their respective ϕ_m (see Sec. III E). Runs extend to $\gamma = 12$, with a single run per condition. The applied shear stress is in the range $0.05\sigma_0 \le \sigma \le 250\sigma_0$. This section displays the collapse of relative viscosity flow-curves for different size ratios for a given scaled area fraction ϕ/ϕ_m. (iii) Section III F presents results for systems with a finite friction coefficient ($\mu = 1$), providing an overview of the rheology at a more realistic frictional state. The small particle area fraction is set at $\zeta = 0.50$.

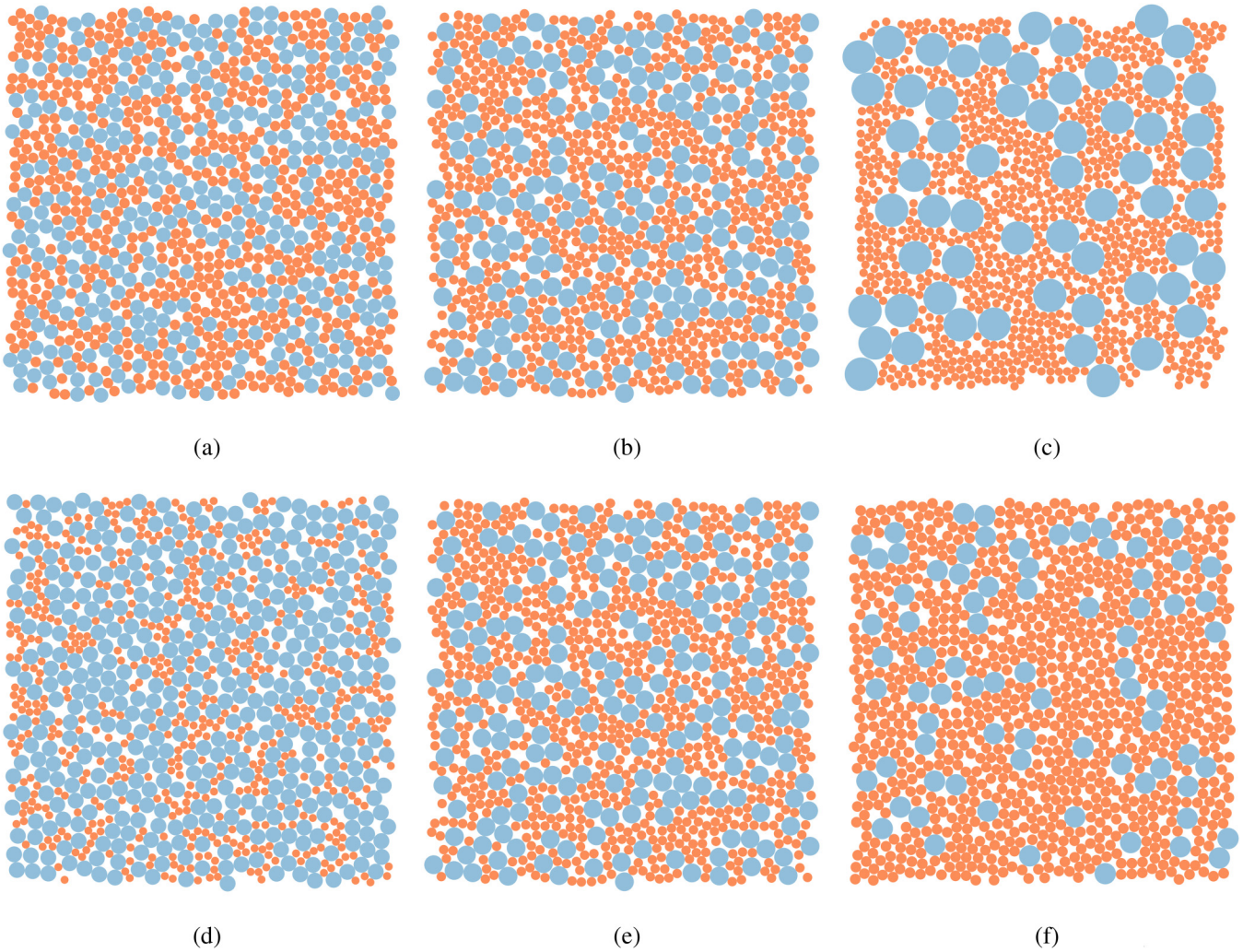

FIG. 1. Overview of bidispersity and small-particle area fraction variations used in this study. All snapshots depict bidisperse systems at total packing fraction $\phi = 0.77$. Top row: Snapshots show varying size ratios δ at a fixed area fraction of small particles of $\zeta = 0.50$. From left to right, the size ratio increases from $\delta = 1.4$ to 4.0. Bottom row: Snapshots showing increasing small-particle area fractions from left to right, ranging from $\zeta = 0.25$ to 0.75, at a fixed size ratio of $\delta = 2.0$. Panel (b) and (e) are essentially the same snapshots. (a) $\delta = 1.4$, $\zeta = 0.50$. (b) $\delta = 2.0$, $\zeta = 0.50$. (c) $\delta = 4.0$, $\zeta = 0.50$. (d) $\delta = 2.0$, $\zeta = 0.25$. (e) $\delta = 2.0$, $\zeta = 0.50$. (f) $\delta = 2.0$, $\zeta = 0.75$.

These simulations cover a range of area fractions and size ratios and are conducted up to $\gamma = 20$, with two replicates per condition. The results are compared directly with corresponding simulations performed at $\mu \to \infty$.

We sample 100 configurations per unit of strain. Statistically steady behavior is reached at $\gamma \approx 0.35$, but data from the entire first strain unit are discarded, with averaging done over the remaining data.

The normal contact forces are modeled as elastic. We choose particle stiffness k_n such that the dimensionless parameter

$$\frac{6\pi\eta_0 a_s \dot{\gamma}}{k_n} \ll 1, \tag{15}$$

and as a result, the maximum particle–particle overlap is approximately 1% for all cases considered.

III. RESULTS

A. Rheological parameters

It is well-established that increasing bidispersity leads to an increase in the jamming area fraction [53], resulting in a lower viscosity at a given solid area fraction. This trend has been observed consistently in experimental studies [54,55] and numerical simulations [15,16]. The primary mechanism underlying this phenomenon is the reduction in the effective excluded volume due to particle size disparity. In a bidisperse suspension, the presence of smaller particles within the interstitial spaces of larger particles allows for a more efficient packing arrangement, allowing flow to continue at larger ϕ. A particularly notable case occurs when the size ratio is $\delta = 4$. In this scenario, the interstitial void formed by four contacting large particles is sufficient to accommodate a smaller particle, further enhancing packing efficiency. The rheological behavior of such suspensions can be described by a power-law relationship of the form

$$\eta_r = k\left(1 - \frac{\phi}{\phi_m}\right)^{-\alpha}, \tag{16}$$

where k is a free parameter. As a result of the power-law relationship from Eq. (16), we may rewrite this as

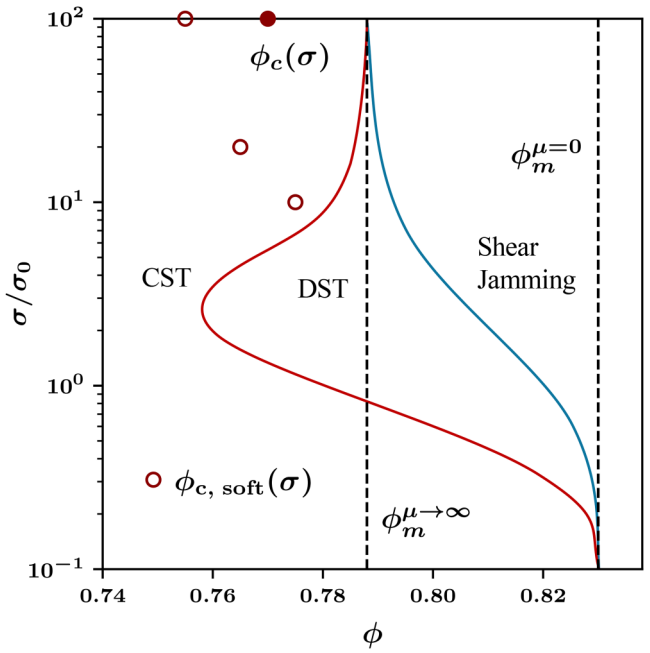

FIG. 2. Flow-state diagram, showing states found (or predicted for ϕ_m) for a 2D suspension for stress σ/σ_0 and area fraction ϕ. To the left of the leftmost (red) curve is the continuous shear-thickening (CST) region, enclosed between the leftmost (red) curve and the rightmost (blue) curve is the discontinuous shear-thickening (DST) region, and the area to the right of the rightmost (blue) curve is shear jamming. Results presented in this article are at $\sigma/\sigma_0 = 100$, a stress above the strong shear-thickening region. The maximum packing $\phi_m^{\mu\to\infty} \approx 0.788$ shown by a dashed line is estimated by fitting mean viscosity information for $\phi < \phi_c$; jamming may occur as low as the critical packing fraction $\phi_c(\sigma)$ (solid circle), where we observe the onset of strong growth of rigid clusters for the current study with hard particles ($\sim$ 1% maximum overlap); $\phi_{c,\mathrm{soft}}(\sigma)$ (open red circles) shows the critical fraction [14] for less rigid particles ($\sim$10% maximum overlap). Values shown for $\delta = 1.4$ and $\zeta = 0.50$.

$$\eta_r^{-1/\alpha} = k^{-1/\alpha} - \frac{k^{-1/\alpha}}{\phi_m} \cdot \phi. \tag{17}$$

Hence, $\eta_r^{-1/\alpha}$ varies linearly with ϕ with a slope of $-k^{-1/\alpha}/\phi_m$, with the intercept at $\eta_r^{-1/\alpha} = 0$ yielding $\phi = \phi_m$. The parameters ϕ_m and k are given in Table I. According to the classic Maron–Pierce [17] equation, the exponent is expected to be 2 and the free parameter to be 1. Our analysis identifies a slightly higher estimate of $\alpha(\mu \to \infty) = 2.42$. The optimal value of α was determined by systematically varying α over a prescribed range and selecting the value that minimized the mean-squared error (Fig. S1 in the supplementary material). For comparison, Fig. S1 (center) also presents the fitting for the case $\alpha = 2$, with detailed fitting parameters provided in Table S1. We report not only relative viscosity but also the particle pressure (Π) and individual normal stresses (Σ_{11} and Σ_{22}) as shown in Fig. 3. Here, particle pressure is defined as the negative mean normal stress $\Pi = -(\Sigma_{11} + \Sigma_{22})/2$.

The parameters ϕ_m and α are estimated by least-square fitting of the time-averaged relative viscosity data to Eq. (17). Refer to Fig. 4 for the viscosity data and least-square fitting for $\zeta = 0.50$ (similar plots for $\zeta = 0.25$ and 0.75 are provided in Fig. S2 of the supplementary material). As noted, the x-intercept in Fig. 4(b) yields the value of ϕ_m, and the y-intercept yields k. As expected, we observe that as the size disparity increases, the predicted viscosity divergence ϕ_m shifts to higher values. However, we will show that large fluctuations associated with the development of rigid clusters cause jamming at values below the predicted ϕ_m.

The rigid particles are identified using the pebble game algorithm described in Sec. II B; the rigid particle fraction m_{rig} within a single simulation configuration and the temporal average of the rigid particle fraction over steady-state samples $\langle f_{\mathrm{rig}} \rangle$ are defined as follows, for N particles in the simulation unit cell:

$$m_{\mathrm{rig}} = \frac{1}{N}\sum_{\mathrm{i}=1}^{N} n_{\mathrm{i}}, \tag{18}$$

$$\langle f_{\mathrm{rig}} \rangle = \frac{1}{t_n}\sum_{\mathrm{i}=1}^{t_n} m_{\mathrm{rig,i}}, \tag{19}$$

where $n_{\mathrm{i}} = 1$ if particle i belongs to a rigid cluster and zero if it does not, and t_n is the total number of such steady-state samples. The average number of frictional contacts per particle in the contact network, excluding particles with no contacts, is denoted by $\langle Z_{net} \rangle$ and defined as

$$\langle Z_{net} \rangle = \frac{1}{t_n}\sum_{\mathrm{i}=1}^{t_n} \frac{Z_{\mathrm{i}}}{N_{z\geq 1}}, \tag{20}$$

where Z_{i} is the total number of frictional contacts in the ith configuration, and $N_{z\geq 1}$ is the total number of particles with frictional contacts.

Figure 5 presents the time-averaged values of the rigid particle fraction $\langle f_{\mathrm{rig}} \rangle$ and frictional contacts per particle $\langle Z_{net} \rangle$, as functions of $\phi - \phi_m$. The parameter f_{rig} exhibits

TABLE I. Fitting parameters of the power law. The fitting parameters for Eq. (17): the maximum jamming fraction ϕ_m and free parameter k for all size ratios and area ratios (δ and ζ) under consideration in this study are mentioned here.

	$\zeta = 0.25$		$\zeta = 0.50$		$\zeta = 0.75$	
δ	ϕ_m	k	ϕ_m	k	ϕ_m	k
1.0	0.787	0.566	0.787	0.566	0.787	0.566
1.4	0.788	0.698	0.787	0.607	0.787	0.577
2.0	0.794	0.832	0.798	0.755	0.792	0.592
4.0	0.828	1.412	0.826	0.941	0.807	0.626

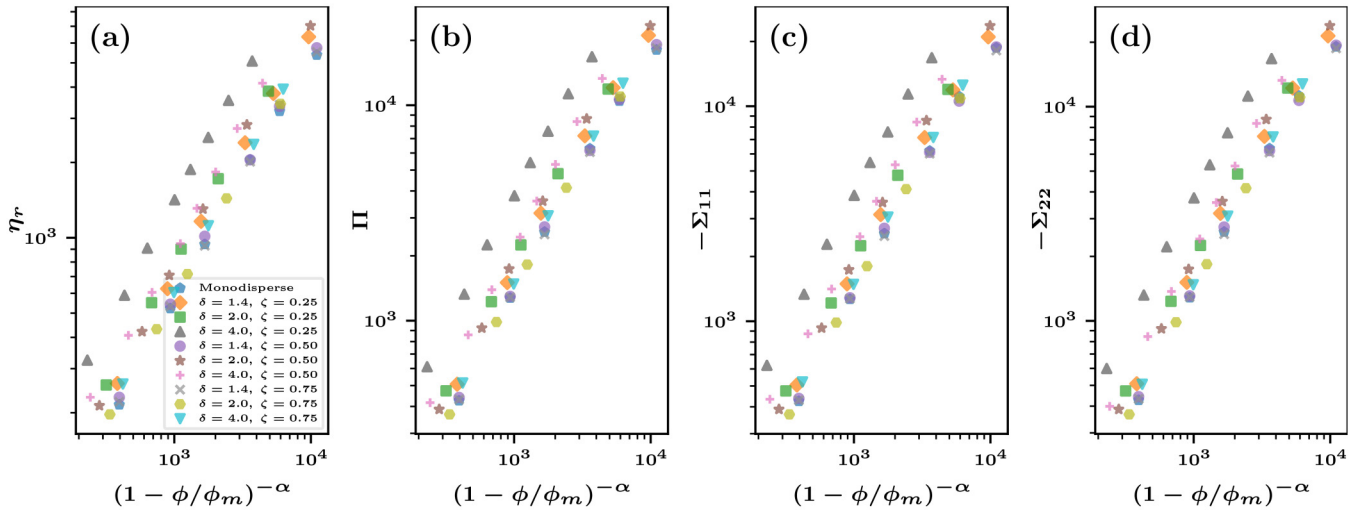

FIG. 3. Variation of rheological parameters with a packing fraction. The rheological parameters—(a) relative viscosity η_r, (b) particle pressure Π, and [(c) and (d)] normal stress components in the 1- and 2-directions (Σ_{11} and Σ_{22})—vary linearly with $(1-\phi/\phi_m)^{-\alpha}$, $\alpha^{\mu\to\infty} = 2.42$. Refer ϕ_m values in Table I. All results are shown at an imposed stress of $\sigma = 100\sigma_0$.

a singular behavior near a critical area fraction ϕ_c, at $\phi_c \approx \phi_m - 0.02$ for the suspension with $\mu \to \infty$. As shown in Fig. 5(b), we observe pronounced fluctuations in the formation of rigid clusters as we approach the critical point ϕ_c, with the fluctuations actually peaking at this ϕ_c. These large fluctuations are suggestive of a second-order phase transition. Recent study by Santra *et al.* [14] demonstrated that f_{rig} grows according to a power-law scaling of the form $f_{\text{rig}} \sim (\phi - \phi_c)^{\kappa}$, with an exponent $\kappa = 1/8$ for $\phi > \phi_c$ similar to the 2D Ising model. Santra *et al.* considered particles softer than those in the current study, with maximum overlaps of $\sim 10\%$ as opposed to $\sim 1\%$ here. They report that fluctuations in the order parameter (m_{rig}) grow sharply, peaking at the critical area fraction ϕ_c, and subsequently decay rapidly as the system approaches the jamming point ϕ_m. This suggests that in the work of Santra *et al.*, for $\phi < \phi_c$, the system is dominated by frictional contacts with smaller overlaps, whereas for $\phi > \phi_c$, time-dependent deformations with larger overlaps allow flow. The mean number of frictional contacts per particle $\langle Z_{net} \rangle$, shown in Fig. 5(c), shows a linear trend with an increase in ϕ, and it approaches the condition of bulk rigidity, $\langle Z_{\text{net}} \rangle \approx 3$, for $\phi \to \phi_m$. In our simulations, we find that when fluctuations to larger values of $m_{\text{rig}} \approx 0.8$ take place in the ϕ_c range, jamming may occur, and thus, the actual jamming fraction is $\phi_J < \phi_m$, with ϕ_m determined by fitting of the time-averaged viscosity data at smaller ϕ. In fact, ϕ_J is quite close to ϕ_c ($\phi_c \lesssim \phi_J$), which we reiterate occurs at the peak of the variance of m_{rig}. Notably, we do not reach the Maxwell threshold for bulk rigidity, $\langle Z_{\text{net}} \rangle = 3$. This is a result of fluctuations in Z_{net}, with specific configurations surpassing the threshold at sufficiently large ϕ. As ϕ approaches the maximum values studied, the standard deviation of the viscosity increases sharply as seen in Fig. 4(c), as do the fluctuations evidenced by the growth of the variance of m_{rig}. Santra *et al.* [14] also demonstrated via finite-size scaling, for $750 \leq N \leq 8000$ in 2D, that the order parameter f_{rig} is controlled by a diverging length scale at the rigidity transition. To assess finite-size effects in our system, we carried out simulations for a subset of system sizes, $N = 500$ and $N = 2000$, and found that the

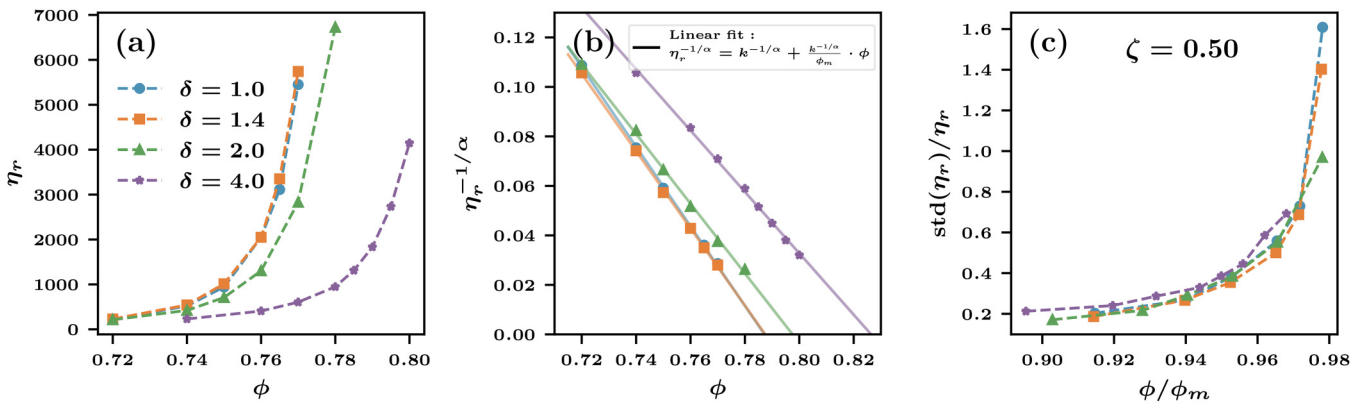

FIG. 4. Relative viscosity and its variance for systems with $\zeta = 0.50$. (a) Relative viscosity η_r and (b) the linear fit for scaled relative viscosity as a function of solid area fraction ϕ. (c) The standard deviation of relative viscosity normalized by the mean value of relative viscosity as a function of scaled solid area fraction ϕ/ϕ_m; ϕ_m values are mentioned in Table I. Here, the exponent $\alpha^{\mu\to\infty} = 2.42$. All results are shown at an imposed stress of $\sigma = 100\sigma_0$.

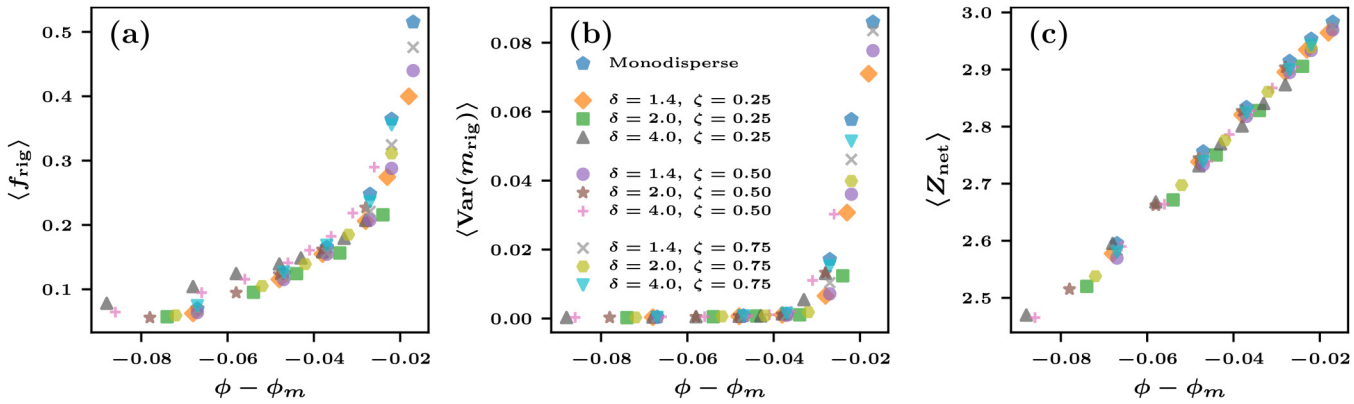

FIG. 5. Order parameters. (a) Rigid particle fraction $f_{\rm rig}$. (b) The variance of $m_{\rm rig}$ increases sharply at the critical packing fraction, $\phi_c \approx \phi_m - 0.02$ here. (c) The mean number of frictional contacts per particle $\langle Z_{net} \rangle$ approach the Maxwell's condition for bulk rigidity $\langle Z_{net} \rangle \sim 3$ close to jamming. The system shows criticality slightly before the maximum packing fraction at $\phi_c = \phi_m - 0.02$. All of the data points show a neat collapse onto a single curve. Refer ϕ_m values in Table I. All results are shown at an imposed stress of $\sigma = 100\sigma_0$.

resulting order parameters roughly fall on those for $N = 1000$ (Fig. S4 in the supplementary material).

Jamming at conditions below the rheologically predicted ϕ_m is not surprising if we consider that this ϕ_m is obtained from the mean viscosity of each simulation fitted to the power-law relation in Eq. (17). This fitting process is inherently agnostic to fluctuations, as it reflects only the trend of the mean. Sufficiently near maximum packing, however, because this is apparently a critical transition [14], fluctuations dominate and ultimately determine whether jamming occurs. The current study, thus, illustrates that the fluctuations are, in fact, related to the process of development of a globally rigid structure from transient finite-size rigid clusters.

B. Contact pair distribution

In a bidisperse system, one has three distinct types of pairwise interactions: small-small (SS), small-large (SL), and large-large (LL). At a fixed small-particle area fraction and N, increasing the size ratio leads to a larger number of small particles and thus a greater number of SS interactions [refer to Fig. 1, panels (a)–(c)]. The contact pair distribution $g(\theta)$ describes the relative probability distribution of frictionally contacting pairs with respect to the angle θ, defined positive counterclockwise from the flow (or x) axis,

$$g(\theta) = \frac{z_\theta}{\bar{z}}, \quad \text{where } \bar{z} = \frac{1}{N_\theta} \sum_{\rm i=1}^{N_\theta} z_{\rm i}, \tag{21}$$

where z_θ is the number of contacts in the bin centered at angle θ and $\bar{z}$ is the mean number of contacts across all $N_\theta = 72$ bins in the θ direction. In Figs. 6(a) and 6(c), both plots are taken at the same relative area fraction $\phi/\phi_m \approx 0.97$, corresponding to $\eta_r \approx 3500$. The angular contact pair distributions g_θ for SS, SL, and LL contacts exhibit similar trends. In Fig. 6(a), we observe a pronounced peak near $\theta = -\pi/4$ (the compression axis) as illustrated in Fig. 6(b). Interestingly, as the bidispersity of the system increases, the contact pair distribution undergoes a noticeable shift. At larger δ, the LL contacts are found to align increasingly along the flow direction, i.e., at $\theta \approx 0$, and this alignment is especially pronounced at higher ζ. In Fig. 6(c), at $\zeta = 0.75$, we observe a sharp peak at $\theta = 0$. Moreover, we also observe a milder peak at $\theta \approx \pi/2$, which indicates that some LL contacts are aligned along the gradient direction, perpendicular to the flow. Figure 6(d) highlights these features, showing the alignment of LL contacts predominantly at $\theta \approx 0$. At higher ζ, and particularly at large δ, the number of large particles decreases, resulting in fewer LL interactions. Details of the total number of contacts for different pair sizes, along with the mean contact number ($\bar{z}$), can be found in the supplementary material: Table S2 provides this information for $\delta = 1.4$ and $\delta = 4.0$.

C. Pair distribution function

We examine the microstructures of the bidisperse systems under consideration by utilizing the pair distribution function (PDF). In a bidisperse system, the PDF for a pair of particles i and j where $i, j =$ small (s) or large (l) is given by

$$g_{i,j}(r, \theta) = \frac{H_{j|i}(r, \theta \mid 0)}{Q}, \tag{22}$$

where

$$H_{j|i}(r, \theta \mid 0) = \frac{N_j}{r \Delta r \Delta \theta}, \tag{23}$$

$$Q = \frac{1}{N_r N_\theta} \sum_{x=1}^{N_r} \sum_{y=1}^{N_\theta} H_{j|i}(r_x, \theta_y \mid 0). \tag{24}$$

Here, $H_{j|i}(r, \theta \mid 0)$ denotes the histogram of bin populations for finding a particle of type j at a distance r and angle θ from a particle of type i. For small–large particle pairs, this quantity is symmetric and also accounts for finding type i around type j. Q represents the mean of the histogram distribution over all bins for a given case, while N_j is the number of particles of type j found in a bin of radial width Δr and

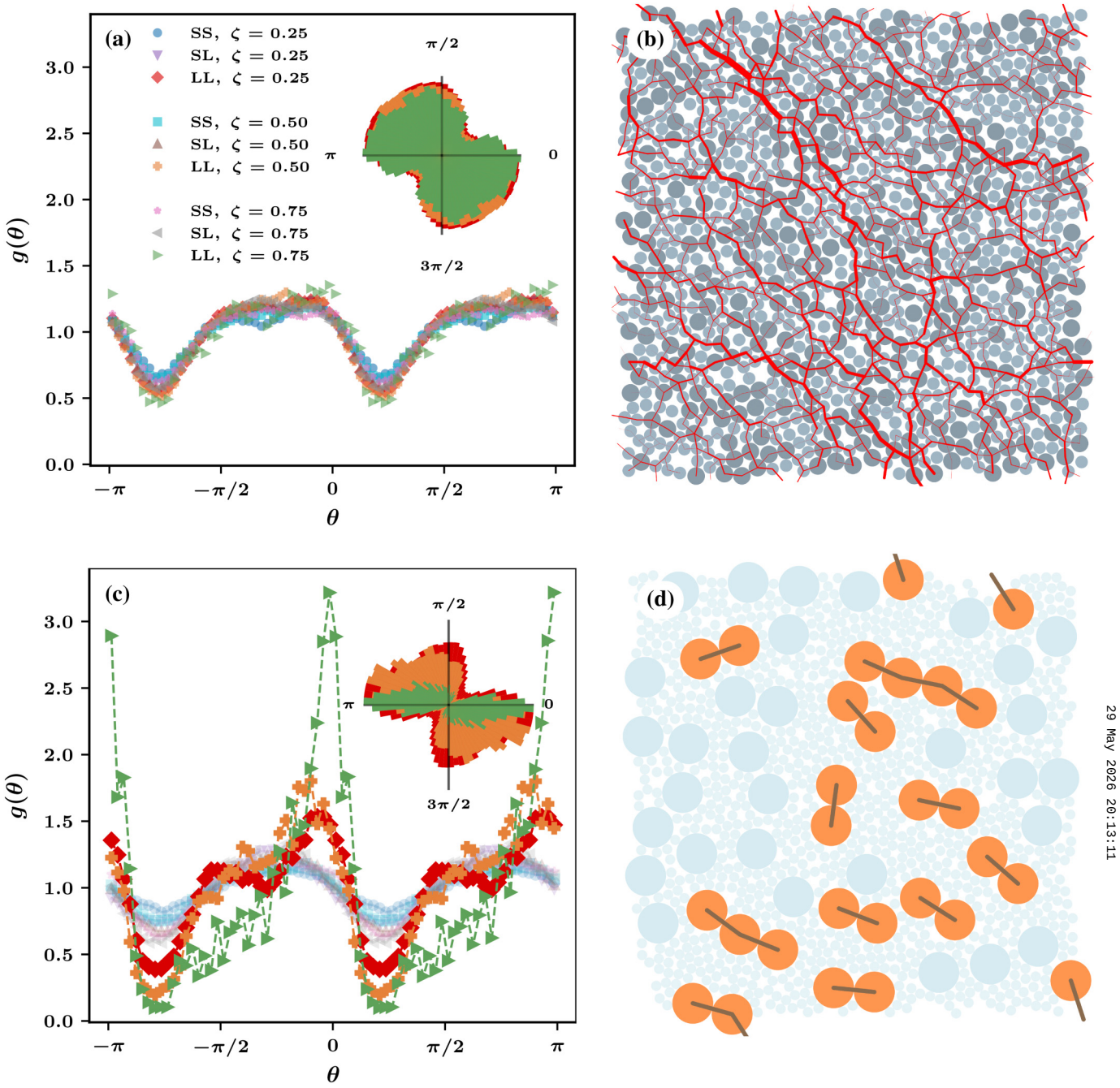

FIG. 6. Angular contact pair probability distributions. Both plots show the contact angle distributions for particle–particle interactions at $\zeta = 0.25, 0.50, 0.75$, with area fractions chosen such that $\phi/\phi_m \approx 0.97$. Distributions are resolved by contact type: SS, SL, and LL. (a) $\delta = 1.4$: Contact angle distributions and (b) a representative snapshot illustrating force chains aligned with the compression axis. We use $\phi = 0.76$ for $\zeta = 0.25$ and 0.50 and $\phi = 0.77$ for $\zeta = 0.75$. (c) $\delta = 4.0$: Contact angle distributions and (d) the corresponding snapshot, highlighting the alignment of large–large contacts along the flow direction ($\theta \sim 0$). Insets show polar histograms (rose diagrams) of LL contacts for the corresponding ζ values. All results are shown at an imposed stress of $\sigma = 100\sigma_0$.

angular width $\Delta\theta$. N_r and N_θ denote the total number of bins in the radial and angular directions, respectively. The pair distribution functions g_{ss}, g_{sl}, and g_{ll} correspond to SS, SL, and LL pairs, respectively, while g_{all} represents the distribution for all pairs in the system, irrespective of size. In this work, we focus on the g_{sl} distribution, as it provides revealing insights.

In Fig. 7, panel (a) and (b) show the PDFs for $\zeta = 0.25$ and $\zeta = 0.75$, respectively, at essentially the same relative viscosity $\eta_r \approx 3500$. The snapshot for $\zeta = 0.25$ in panel (c) shows long chains for the SL contact network, whereas for $\zeta = 0.75$ [panel (d)], we see SL contacts being concentrated around the relatively fewer larger particles. We can identify a compression axis and an extension axis in the PDF from panel (b) as compared to PDF from panel (a), and the same can also be observed from panel (d) where the SL contacts are more aligned along the compression axis ($\theta \approx -\pi/4$). The radial contact distribution $g(r)$ given in panel (e) shows clearly the probability peaks with distance. We see sharper peaks for $\zeta = 0.75$ due to equally spaced large particles in

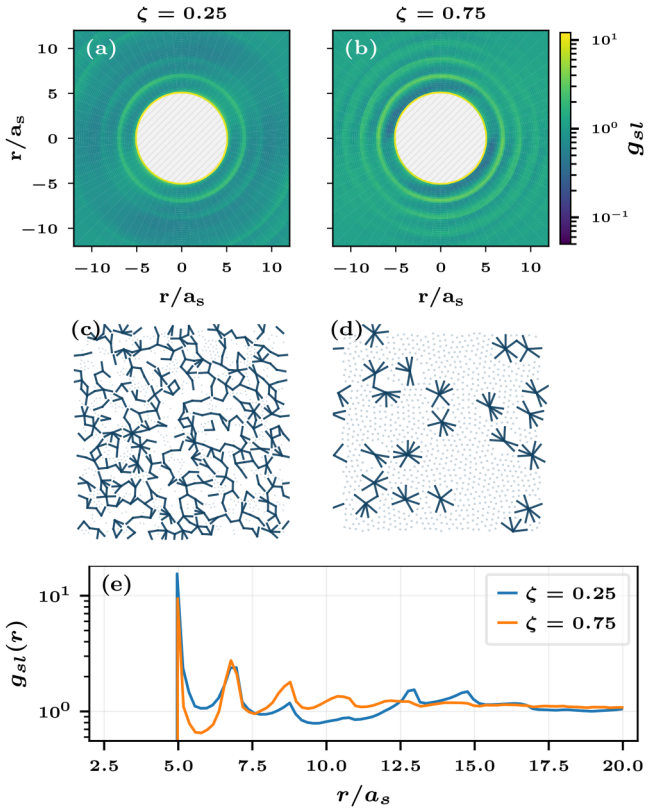

FIG. 7. PDF. All figures are for $\delta = 4.0$ and compare the small-large (SL) contact network distribution (g_{sl}). All plots here are at similar relative viscosity ($\eta_r \sim 3500$). (a) The PDF and (c) SL contact network snapshot for a frame for $\zeta = 0.25$ and $\phi = 0.795$. (b) The PDF and (d) SL contact network snapshot for a frame for $\zeta = 0.75$ and $\phi = 0.795$. (e) Radial distribution function for SL contacts for the same two cases shown in (a) and (b). Results are shown for $\sigma = 100\sigma_0$.

the system, whereas for $\zeta = 0.25$, the large and small particles are more homogeneously distributed.

D. Rigid clusters and shear jamming

A group of particles that acquires sufficient constraints to eliminate all internal degrees of freedom, leaving only translational and rotational motion of the entire group, is termed a *rigid cluster*. Here, such clusters are identified using the pebble game algorithm, as described in Sec. II B. A PG-identified rigid cluster consists of a minimum of three particles, and as the number of interacting particles increases, the degrees of freedom of a greater number of particles are constrained, ultimately forming larger rigid clusters. These clusters become large enough that they can no longer translate or rotate under a constant-volume shear flow, leading to *shear jamming*. Shear jamming occurs when the repulsive σ_r and contact σ_c stresses balance the imposed stress such that

$$\sigma = \sigma_r + \sigma_c, \tag{25}$$

indicating that no hydrodynamic stress, and thus no shearing, is required. Operationally, in our simulations, we determine the occurrence of shear jamming as the event when $\sigma_r + \sigma_c > \sigma$, which from Eq. (10) implies a negative shear rate.

In Fig. 8, particles identified as belonging to rigid clusters by the PG algorithm are highlighted in red across various sampled configurations. Rows 1–3 correspond to area fractions of $\phi = 0.76$, $\phi = 0.765$, and $\phi = 0.77$, respectively, all at the same $\sigma = 100\sigma_0$. From left to right, the snapshots evolve in time, indicating the fluctuating nature of the rigid particle fraction. We observe that the sizes of the rigid clusters are relatively smaller for lower ϕ. The final column in Fig. 8 presents the distribution of particles in rigid clusters at each sampling, i.e., the distribution of m_{rig} from Eq. (18), given by $P_{m_{\text{rig}}}$. Panel (k) in Fig. 8, highlighted with a red box, shows the shear-jammed configuration. At $\phi = 0.76$, the clusters are predominantly small in size. However, as the area fraction increases, we observe some probability of large clusters, and for $\phi = 0.77$, a bimodal distribution of m_{rig} emerges. As noted above, there is a finite probability of jamming when the bimodal distribution appears, a point that was not clear in examination of similar issues with softer particles [13,14].

In our simulations, we observe shear-jamming events for monodisperse suspensions at $\phi = 0.765$ and 0.77; bidisperse suspensions at $\phi = 0.77$, $\zeta = 0.25$ with $\delta = 1.4$ and 2.0; and at $\phi = 0.78$, $\zeta = 0.50$ with $\delta = 2.0$; note that this means one in two simulations jams by a strain of $\gamma = 20$. These events occur at $\phi/\phi_m \sim 0.97$, when fluctuations lead to m_{rig} being large, as indicated in Fig. 8(l), where the jamming case is marked by a dashed red line at $m_{\text{rig}} \sim 0.85$, corresponding to the configuration of Fig. 8(k), although the first rigidity percolation occurs in the range 0.95 (for $\delta = 4.0$) $\leq \phi/\phi_m \leq 0.97$ (for $\delta = 1.0$). The configurations with percolating rigid clusters have $\langle m_{\text{rig}} \rangle_{\,percolating} \gtrsim 0.80$. We present $P_{m_{\text{rig}}}$ plots for other cases in Fig. S5 of the supplementary material.

In Fig. 9, we present the time series plots for cumulative strain γ, normalized shear rate $\dot{\gamma}/\dot{\gamma}_0$, relative viscosity η_r, and the mean number of frictional contacts per particle $\langle Z_{\text{net}} \rangle$. The vertical red dashed line marks the jamming point, obtained by our operational definition when $\dot{\gamma}/\dot{\gamma}_0 < 0$. At this jamming point, we observe $\langle Z_{\text{net}} \rangle \approx 3.1$ [Fig. 9(d)], slightly above the Maxwell threshold for bulk rigidity. We see that there are other time points where η_r grows sharply as the shear rate falls steeply (while remaining positive), implying a near-jamming event. One such instance occurs later in the time series, at $t\dot{\gamma}_0 \approx 1000$, where $\dot{\gamma}$ exhibits a sharp dip accompanied by peaks in both η_r and $\langle Z_{\text{net}} \rangle$. Such near-jamming events highlight the fluctuation-dominated nature of the flow close to jamming, as shown in the experimental work by Lootens *et al.* [56].

E. Rate-dependent viscosity

The system flow curve is generated by conducting simulations at varying imposed shear stress. The area ratio is fixed at $\zeta = 0.50$, and the area fractions are chosen such that $\phi/\phi_m \approx 0.97$. Specifically, we select $\phi = 0.765$ for $\delta = 1.0$ and 1.4, $\phi = 0.77$ for $\delta = 2.0$, and $\phi = 0.795$ for $\delta = 4.0$. The values of ϕ_m in Table I are reported for a stress of $\sigma = 100\sigma_0$. Each simulation is performed for a total strain of $\gamma = 12$, with the initial unit strain discarded to ensure that

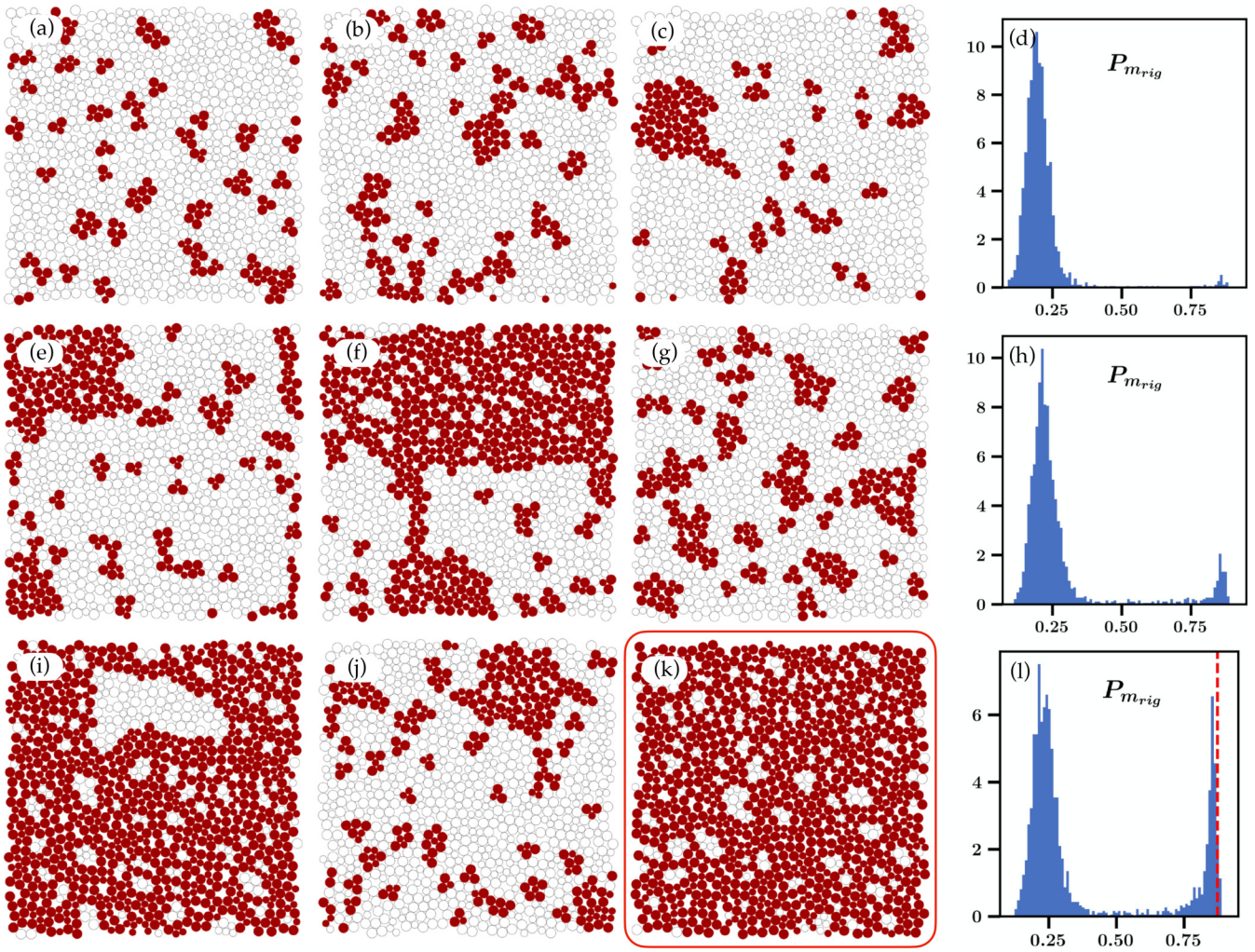

FIG. 8. Approach to shear jamming with an increase in the area fraction. Panels (a)–(c), (e)–(g), and (i)–(k) show simulation snapshots, where particles belonging to the rigid cluster (as identified by the pebble game) are highlighted by solid (red) circles. The corresponding density distributions of the rigid particle fraction, $P_{m_{\text{rig}}}$, are presented in the last column in panels (d), (h), and (l). Each row represents the snapshots and $P_{m_{\text{rig}}}$ for $\phi = 0.76$, 0.765, and 0.77, respectively ($\delta = 1.4$ and $\zeta = 0.25$ for all three cases of area factions). Panel (k), highlighted with a red box, shows the frame in which jamming occurs and system-spanning rigid clusters form. The snapshots evolve in time from left to right. All results are shown at an imposed stress of $\sigma = 100\sigma_0$.

only steady-state statistics are included in the analysis. Compared to other studies in this paper, where $\gamma = 20$ and two independent runs are considered for each case, here, we adopt a shorter duration and a single run for each case as this proves sufficient to characterize the flow curves.

From Fig. 10(a), we observe a characteristic shear-thinning behavior at low stress levels. In this regime, particle interactions are primarily governed by repulsive and hydrodynamic forces, and frictional contacts between particles are negligible. As the applied stress increases, the system reaches a critical stress beyond which the repulsive forces are overcome, leading to the onset of frictional contacts. This transition results in an increase in flow resistance as more frictional contacts are activated. The minima of the flow curves occurs at a stress $\approx 0.5\sigma_0$. A notable feature in the flow curve is a sharp decrease in viscosity for the $\delta = 1.0$ (monodisperse) case at this minimum; this reduction in flow resistance can be attributed to particle layering. For the monodisperse case, the particles tend to organize into layers parallel to the flow direction, reducing the effective viscosity before further increases in stress lead to the activation of additional frictional contacts. The first normal stress difference, $N_1 = \Sigma_{11} - \Sigma_{22}$, exhibits distinct trends across different size ratios. At lower stress values, N_1 is near zero. However, as the imposed stress increases beyond $\sigma/\sigma_0 \approx 1$, a negative normal stress difference emerges for the highly bidisperse cases of $\delta = 4.0$.

F. Anisotropy in frictional systems

Here, we compare results from simulations with finite friction coefficient ($\mu = 1$) and for $\mu \to \infty$. The rheological parameters for $\mu = 1$ are provided in Fig. S8 of the supplementary material. We focus exclusively on the bidisperse systems with $\delta = 1.4$, 2.0, 4.0 at $\zeta = 0.50$. A fit of the relative viscosity, as given by Eq. (17), is considered. The optimum scaling exponent for $\mu = 1$ is found to be $\alpha_{\text{opt}}(\mu = 1) = 1.71$ (Fig. S7), whereas $\alpha_{\text{opt}}(\mu \to \infty) = 2.42$ (Table S3). Traditionally, the relative viscosity exponent is assumed to be $\alpha = 2$, as proposed by Maron and Pierce [17].

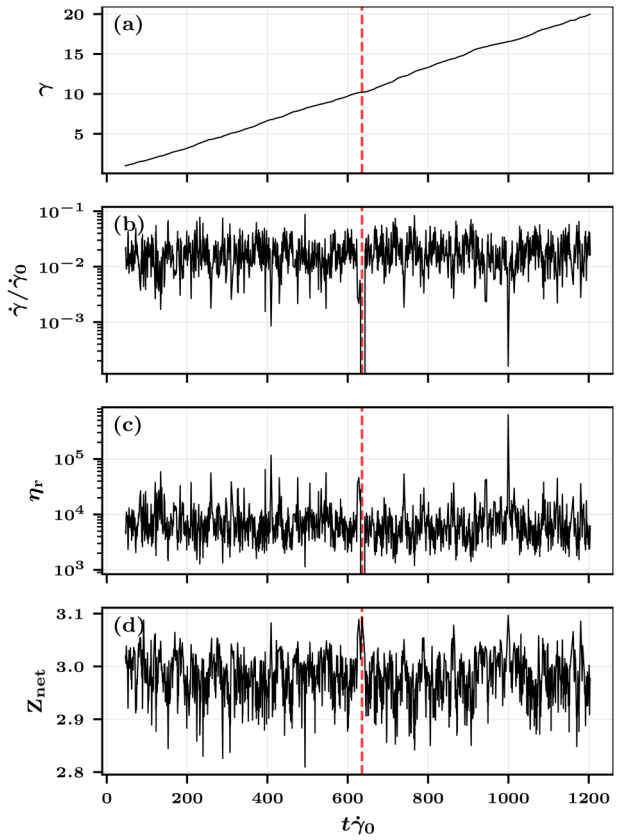

FIG. 9. Time series near the jamming point. Time series for (a) cumulative strain (b) normalized shear rate (c) viscosity (d) frictional contacts per particle. The plots shown are for the case with $\phi = 0.77$, $\zeta = 0.25$ and $\delta = 1.4$, similar to the case shown in Fig. 8, Row 3. The vertical red dashed line at $t\dot{\gamma}_0 \sim 620$ is where we observe the event of shear jamming (i.e., $\dot{\gamma}/\dot{\gamma}_0 < 0$). All results are shown at an imposed stress of $\sigma = 100\sigma_0$.

However, our results indicate that the optimum exponent depends on the friction coefficient μ. The fits of the relative viscosity provide estimates of ϕ_m and the free parameter k, with values summarized in Table S3 (for cases with $\mu = 1$).

Structural anisotropy in granular media is an important parameter to understand the contact network [57], stress transmission though force chain networks [58,59], and macroscopic properties, such as dilatancy [60,61] and bulk modulus [62]. The fabric tensor is often used to quantify the anisotropy. We define the force-weighted fabric tensor as [63]

$$\mathbf{F} = \frac{1}{\sum_c^{N_c} f_c} \sum_{c=1}^{N_c} f_c \, \mathbf{n}^{(c)} \otimes \mathbf{n}^{(c)}, \tag{26}$$

where f_c is the magnitude of the normal contact force, N_c is the number of contacts in the configuration, and $\mathbf{n}^{(c)}$ is the contact vector going from the ith particle to the jth particle. We determine the eigenvalues λ_k of the fabric tensor from

$$\mathbf{F}\cdot\mathbf{v}_k = \lambda_k \, \mathbf{v_k}, \quad k = 1 \text{ or } 2, \tag{27}$$

where $\mathbf{v}_k$ are the eigenvectors giving the principal directions of contact anisotropy. The anisotropy is quantified by [64]

$$A = 1 - \frac{\lambda_{\min}}{\lambda_{\max}}, \tag{28}$$

where $A = 0$ corresponds to an isotropic system, while $A = 1$ represents maximal anisotropy. Figure 11 illustrates the variation of A with increasing ϕ for both frictional cases. We report the temporal mean of anisotropy, $\langle A \rangle$, computed over steady-state configurations. The results indicate that systems with lower friction coefficients develop more anisotropic structures. Among the bidisperse cases, $\delta = 4.0$ exhibits comparatively weaker anisotropy than the smaller size ratios, for all of which $\langle A \rangle$ is quite similar. The degree of anisotropy obtained from the fabric tensor without force information (Fig. S10 in the supplementary material) exhibits a similar trend to that estimated with force information, but this purely

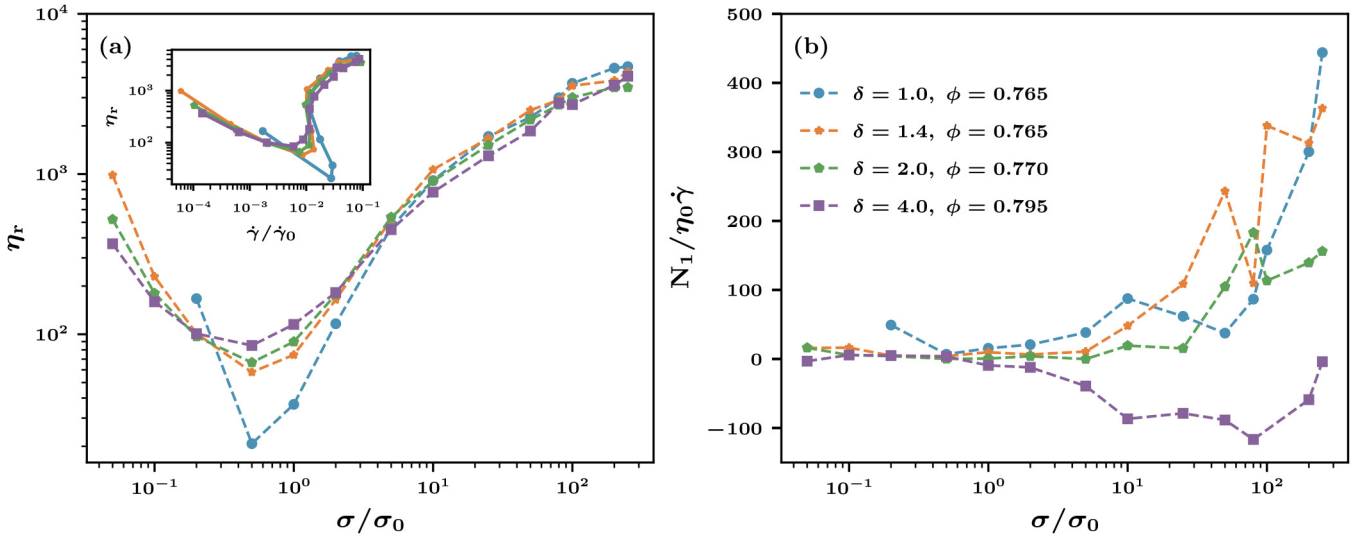

FIG. 10. Rate dependence of viscosity and a first normal stress difference. (a) The flow curves for the relative viscosity of all bidisperse cases at a fixed area fraction, $\phi/\phi_m \approx 0.97$, where ϕ_m is estimated at high stress (values given in Table I). The small-particle fraction is fixed at $\zeta = 0.50$. The inset highlights the viscosity variation with nondimensional shear rate, illustrating the transition from lubricated to frictional contacts. (b) The first normal stress difference at different imposed stress values.

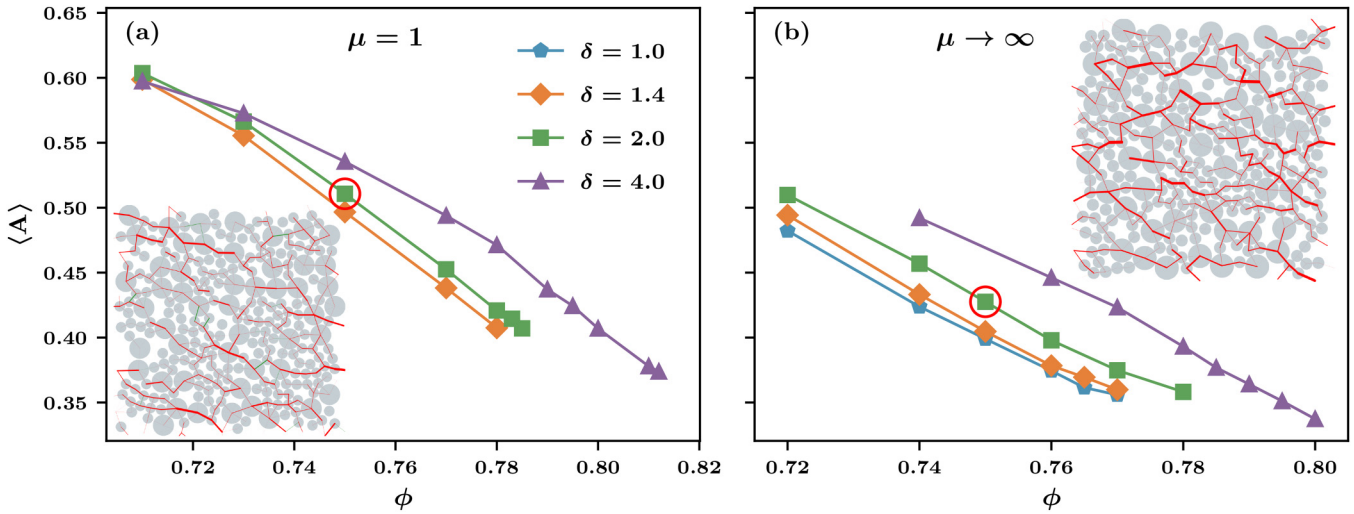

FIG. 11. Contact anisotropy. The anisotropy as characterized by A, defined in terms of the fabric tensor eigenvalues, is shown for (a) finite ($\mu = 1$) and (b) infinite ($\mu \to \infty$) friction coefficients. Inset: System snapshots at $\phi = 0.75$ and $\delta = 2.0$, corresponding to the data points highlighted in red circle in both plots. Each snapshot represents a zoomed-in subset of a larger system ($N = 1000$) for visual clarity. Nonsliding contacts are shown in red and sliding contacts in green (if viewed online), with line thickness indicating the magnitude of the combined normal and tangential forces. Sliding contacts appear only for $\mu = 1$ since no sliding occurs at infinite friction. Line thickness is scaled relative to the maximum force within each snapshot and is, therefore, not directly comparable between the two cases. All results are shown at an imposed stress of $\sigma = 100\sigma_0$.

contact anisotropy is weaker. This suggests that the contact fabric itself encodes aspects of friction, consistent with observations in experimental studies [65], and also affects the interaction with the imposed flow as indicated by the magnitude of the force, f_c.

We also examine the order parameters in the $\mu = 1$ suspension (Fig. S10 in the supplementary material). The order parameter f_{rig}, the variance of m_{rig}, and $\langle Z_{net} \rangle$ are of comparable magnitude to those observed in the infinite-friction case. A key distinction, however, is that with lower friction, flow is possible much closer to the ϕ_m. This difference appears to arise from the reduced fluctuations at $\mu = 1$, borne out in the fluctuations in η_r, which are significantly larger for $\mu \to \infty$ [Fig. 4(c)] than for $\mu = 1$ (Fig. S9, right panel).

IV. CONCLUSIONS

This study has used the established simulation approach, LF-DEM [12,13], to examine the rheology, contact dynamics, and structural fabric of dense bidisperse suspensions in two dimensions, modeled as a monolayer of spheres under simple shear flow. We have considered the effects of particle size ratio, area fraction, and small-particle fraction. The LF-DEM framework successfully captures shear-thinning and shear-thickening behavior, as illustrated in Fig. 10. The 2D suspension has rheology that is phenomenologically similar to the 3D case [14] and has the advantage that the pebble game algorithm [51,52] allows rigorous analysis of rigid structures in the contact network. A key finding of this work is that the development of global rigidity at jamming occurs through a critical process, in which the key mechanism is the development of transient rigid clusters, which grow sharply while exhibiting strong fluctuations in size at a critical solid fraction ϕ_c. Because the clusters can percolate when a fluctuation that results in a large fraction of the particles being in rigid clusters (denoted m_{rig}), the fluctuations of the state of the material become intense in this near-jamming regime. We find that jamming can take place when system-spanning rigid clusters begin to appear, which is typically seen at $m_{\text{rig}} \geq 0.77$. The jamming probability increases as ϕ approaches $\phi_c \approx \phi_m - 0.02$ for the case of $\mu \to \infty$ and for $\mu = 1$, $\phi_c \approx \phi_m - 0.01$. Thus, jamming can occur at solid fraction substantially below ϕ_m, the maximum flowable fraction predicted based upon correlations of the time-averaged viscosity at smaller ϕ. These results are found to be general across the range of mono- and bidisperse suspensions studied here, although the structural anisotropy is found to become significantly weaker for the bidispersity cases studied (with small particle fraction $\zeta = 0.25$–0.75) for a size ratio of $\delta = 4$.

Prior studies have often used traditional constitutive models, such as the Maron–Pierce relation [17], to describe the relative viscosity behavior of a dense suspension, adopting a fixed exponent $\alpha = 2$ for the form $\eta_r \sim (1 - \phi/\phi_m)^{-\alpha}$. In contrast, we use an empirical power-law shown in Eq. (17), allowing α to vary and determine its optimal value by minimizing the mean-squared error across a range of α. We find that α is not universal but instead depends on the friction coefficient: $\alpha(\mu \to \infty) = 2.42$ and $\alpha(\mu = 1) = 1.71$. Importantly, even if α were fixed at the Maron–Pierce value of 2, the resulting estimates of ϕ_m remain close to those obtained from the optimized fit (refer Tables S1 and S3 in the supplementary material). This indicates that the fitted ϕ_m, which is the primary quantity of interest, is relatively insensitive to the precise choice of α. In many of the results presented in this paper, the case with $\delta = 4.0$ shows behavior that is distinct from the lower size-ratio cases. The monodisperse and bidisperse systems with $\delta = 1.4$ behave very similarly, validating the use of this level of bidispersity as a means of maintaining an

amorphous structure while capturing the behavior of nearly monodisperse suspensions.

We have analyzed the particle contact distributions in both angular and radial directions. At low bidispersity ($\delta = 1.4$), most contacts align with the compression axis ($\theta = -\pi/4$ or $3\pi/4$ from the flow axis). In contrast, at higher bidispersity ($\delta = 4.0$), large–large (LL) contacts exhibit a pronounced reorientation, preferentially aligning with the flow direction ($\theta \approx 0$). This effect is amplified with increasing small-particle area fraction (ζ), as LL pairs progressively align with the flow. A secondary peak near $\theta = \pi/2$ further indicates clustering perpendicular to the flow. Overall, the contact pair distributions demonstrate that both the size ratio (δ) and the small-particle fraction (ζ) play critical roles in reorganizing the preferred contact orientations. A similar phenomenon is observed in simulations of 3D suspensions, where large interacting particles form layers with normals aligned along the velocity gradient under high stress [16].

The onset of shear jamming is investigated using a graph-theoretical framework, based on the PG. The PG detects rigid substructures in the contact network by counting constraints relative to available degrees of freedom, enabling a quantitative description of rigidity emergence in dense suspensions. The transition to shear jamming occurs within a narrow range of packing fractions. At $\phi = 0.77$ ($\delta = 1.4$, $\zeta = 0.25$), we observe a distinct bimodal distribution in the rigid fraction m_{rig}, whereas at $\phi = 0.76$, the m_{rig} distribution remains unimodal. This abrupt change is indicative of critical behavior. Consistent with this, the variance of m_{rig} grows sharply near jamming, a hallmark of second-order phase transitions. The fluctuation in relative viscosity also rises rapidly as ϕ increases near the jamming condition. We have defined ϕ_m through a fitting of the viscosity data, and in our simulations, the jamming event consistently occurs at $\phi < \phi_m$. This discrepancy arises because ϕ_m is obtained from a fit of Eq. (17) to average viscosity data, which neglects fluctuations. As a result, the fitted ϕ_m reflects only the mean trend, while the variance of the viscosity near jamming indicates that there is a range of ϕ where jamming may occur, with the probability clearly increasing with ϕ as shown in Seto *et al.* [30]. Close to jamming, fluctuations dominate and this makes ϕ_m unreliable as an actual jamming point. Particle properties also play a role: friction promotes earlier onset of rigidity, while particle softness delays it. We hypothesize that more rigid particles undergo shear jamming at lower ϕ, whereas softer particles deform and overlap, reducing their effective area fraction and thereby delaying jamming. Our preliminary simulations are consistent with this hypothesis, although further work is needed to confirm it.

At lower packing fractions, we observe small, isolated rigid clusters. As the packing fraction increases, these clusters grow in size, and at a certain area fraction, we observe the first signatures of system-spanning rigid clusters, and typically at this packing fraction, such instances are few. At sufficiently high packing fraction, ϕ_c, we begin to see much higher instances of system-spanning or percolating rigid clusters. These are clear indicators that at this ϕ, because of large fluctuations in m_{rig}, a finite probability of jamming exists: a condition that exhibits percolating rigid clusters can eventually jam when sheared for sufficiently large strain. We observe the occurrence of jamming point ϕ_J near ϕ_c. At a slightly higher packing fraction, we find the maximum packing fraction ϕ_m as predicted by the power-law fit [Eq. (17)]. For example, for the case of $\delta = 1.4$ and $\zeta = 0.75$ (at $\mu \to \infty$), the first system-spanning rigid clusters appear at $\phi = 0.76$, and the onset of large variation in the fraction of particles in rigid clusters is at $\phi_c = 0.765 \approx \phi_m - 0.02$, while a shear-jamming event occurs at $\phi_{\mathrm{J}} = 0.78$. However, the jamming fraction may be closer to ϕ_c, and given the estimated $\phi_m = 0.787$ (refer Table I), the apparent situation is that $\phi_c \lesssim \phi_{\mathrm{J}} < \phi_{\mathrm{m}}$. In comparison with the work of Santra *et al.* [14], where the full fluctuating regime was accessible for the softer particles (i.e., the variance of m_{rig} went through a definite peak and came down), here, the large fluctuations with harder particles can lead to jamming, and the most extreme fluctuating behavior may be cut off.

We also present flow curves for different size ratios over a stress range of $0.05\sigma_0 \leq \sigma \leq 250\sigma_0$, plotted against the area fraction normalized by the maximum packing fraction, ϕ/ϕ_m. The value of ϕ_m is estimated at $\sigma = 100\sigma_0$. When scaled by this ϕ_m, the flow curves collapse onto a master curve, except for the monodisperse case ($\delta = 1.0$) at low shear stress. The deviation in this case arises from particle ordering, as confirmed by simulation snapshots (see the movie attached as part of the supplementary material). As a result of the ordering, the N_1 value decreases to near zero at this point. In the highly bidisperse case ($\delta = 4.0$), N_1 becomes strongly negative, indicating enhanced isotropic structuring in the suspension, consistent with the reduced anisotropy discussed in Sec. III F. The force chain structure responsible for transmitting stresses is more anisotropic for the systems with low friction. In summary, the friction coefficient dictates the viscosity exponent α, accuracy of the maximum packing point, and degree of anisotropy.

Our two-dimensional simulations show trends consistent with three-dimensional studies and allow analysis of microstructures driving shear jamming. The linear fit for relative viscosity provides a reliable model across a wide range of area fractions, size ratios, and compositions. Importantly, while a direct observation of rigid clusters in experiments is challenging, our finding that viscosity variance reflects the system state offers a powerful and often overlooked feature, potentially guiding future experimental work. The preferential layering of large particles, also reported in 3D simulations, has practical relevance for industrial processes, such as food and pharmaceutical mixing, where homogeneity is critical. Finally, we demonstrate a robust collapse of the flow curve based on ϕ_m at high shear rates, extending predictive capability to other size ratios, and show that anisotropy derived from contact fabric, whether or not force information is included, tracks the bulk frictional state.

SUPPLEMENTARY MATERIAL

The supplementary material provides additional information supporting the main text. It includes the optimum α values obtained by minimizing the mean-squared error (MSE) for the linear fit using Eq. (17), for $\mu \to \infty$ (Fig. S1)

and $\mu = 1$ (Fig. S7). It also includes the finite-size consistency plot for f_{rig} (Fig. S4). Additional plots of the density distribution of rigid particles $P_{m,\text{rig}}$ and order parameters (f_{rig} and z_{net}) for other jammed cases encountered in the study are shown in Figs. S5 and S6. Rheological data for $\mu = 1$ are presented in Fig. S8. Fit parameters ϕ_m and k for all cases considered are tabulated in Tables S1 ($\mu \to \infty$, only for $\alpha = 2$) and S3 ($\mu = 0$). The comparison of anisotropy for the finite- and infinite-friction cases is shown in Figs. S10 (as a function of packing fraction ϕ) and S11 (as a function of scaled packing fraction ϕ/ϕ_m). An attached supplementary movie illustrates the ordering of the monodisperse systems under low shear stress, which leads to a drop in viscosity at $\sigma = 0.5\sigma_0$.

ACKNOWLEDGMENTS

The authors gratefully acknowledge support from the National Science Foundation (NSF) grants (CBET 2228680, CBET 2228681, and CBET 2333223). The authors thank Professor Eric Weeks for many helpful discussions. Computational resources were provided in part by the CUNY High Performance Computing Center at the College of Staten Island, supported by NSF Awards (CNS-0958379, CNS-0855217, ACI-1126113, and OAC-2215760). Additional resources were provided by the DARWIN computing system—A Resource for Computational and Data—Intensive Research at the University of Delaware—through Allocation No. CHM240064 from the Advanced Cyberinfrastructure Coordination Ecosystem: Services and Support (ACCESS) program, which is supported by NSF Awards (2138259, 2138286, 2138307, 2137603, and 2138296) [66,67].

AUTHOR DECLARATIONS

Conflict of Interest

The authors have no conflicts to disclose.

DATA AVAILABILITY

Raw data were generated at the CUNY High Performance Computing Center and DARWIN computing system facilities. Derived data supporting the findings of this study are available from the corresponding author upon reasonable request.

REFERENCES

[1] Sharma, A., S. Gupta, M. Noman Husain, and S. Chaudhary, "Factors affecting the rheology of cement-based composites: A review," J. Am. Ceram. Soc. **108**, e20429 (2025).

[2] Mandal, R., S. K. Panda, and S. Nayak, "Rheology of concrete: Critical review, recent advancements, and future prospectives," Constr. Build. Mater. **392**, 132007 (2023).

[3] Cheng, H., S. Wu, H. Li, and X. Zhang, "Influence of time and temperature on rheology and flow performance of cemented paste backfill," Constr. Build. Mater. **231**, 117117 (2020).

[4] Bugday, Z. Y., A. Venkatachalam, P. D. Anderson, and R. G. M. van der Sman, "Rheology of paste-like food inks for 3D printing: Effects of nutrient and water content," Curr. Res. Food Sci. **9**, 100847 (2024).

[5] Vásquez, C., G. Henríquez, J. V. López, E. K. Penott-Chang, A. J. Sandoval, and A. J. Müller, "The effect of composition on the rheological behavior of commercial chocolates," LWT **111**, 744–750 (2019).

[6] De Graef, V., F. Depypere, M. Minnaert, and K. Dewettinck, "Chocolate yield stress as measured by oscillatory rheology," Food Res. Int. **44**, 2660–2665 (2011).

[7] Kostynick, R., H. Matinpour, S. Pradeep, S. Haber, A. Sauret, E. Meiburg, T. Dunne, P. Arratia, and D. Jerolmack, "Rheology of debris flow materials is controlled by the distance from jamming," Proc. Natl. Acad. Sci. U.S.A. **119**, e2209109119 (2022).

[8] Finnegan, N. J., and D. M. Saffer, "Seasonal slow slip in landslides as a window into the frictional rheology of creeping shear zones," Sci. Adv. **10**, eadq9399 (2024).

[9] Chevrel, M., T. Platz, E. Hauber, D. Baratoux, Y. Lavallée, and D. B. Dingwell, "Lava flow rheology: A comparison of morphological and petrological methods," Earth Planet. Sci. Lett. **384**, 109–120 (2013).

[10] Lev, E., M. Spiegelman, R. J. Wysocki, and J. A. Karson, "Investigating lava flow rheology using video analysis and numerical flow models," J. Volcanol. Geotherm. Res. **247–248**, 62–73 (2012).

[11] Wyart, M., and M. E. Cates, "Discontinuous shear thickening without inertia in dense non-Brownian suspensions," Phys. Rev. Lett. **112**, 098302 (2014).

[12] Mari, R., R. Seto, J. F. Morris, and M. M. Denn, "Shear thickening, frictionless and frictional rheologies in non-Brownian suspensions," J. Rheol. **58**, 1693–1724 (2014).

[13] van der Naald, M., A. Singh, T. T. Eid, K. Tang, J. J. de Pablo, and H. M. Jaeger, "Minimally rigid clusters in dense suspension flow," Nat. Phys. **20**, 653–659 (2024).

[14] Santra, A., M. Orsi, B. Chakraborty, and J. F. Morris, "Rigid clusters in shear-thickening suspensions: A nonequilibrium critical transition," Phys. Rev. Res. **7**, 013275 (2025).

[15] Pednekar, S., J. Chun, and J. F. Morris, "Bidisperse and polydisperse suspension rheology at large solid fraction," J. Rheol. **62**, 513–526 (2018).

[16] Malbranche, N., B. Chakraborty, and J. F. Morris, "Shear thickening in dense bidisperse suspensions," J. Rheol. **67**, 91–104 (2023).

[17] Maron, S. H., and P. E. Pierce, "Application of Ree-Eyring generalized flow theory to suspensions of spherical particles," J. Colloid Sci. **11**, 80–95 (1956).

[18] Lobry, L., E. Lemaire, F. Blanc, S. Gallier, and F. Peters, "Shear thinning in non-Brownian suspensions explained by variable friction between particles," J. Fluid Mech. **860**, 682–710 (2019).

[19] Vázquez-Quesada, A., R. I. Tanner, and M. Ellero, "Shear thinning of noncolloidal suspensions," Phys. Rev. Lett. **117**, 108001 (2016).

[20] Madraki, Y., A. Oakley, A. Nguyen Le, A. Colin, G. Ovarlez, and S. Hormozi, "Shear thickening in dense non-Brownian suspensions: Viscous to inertial transition," J. Rheol. **64**, 227–238 (2020).

[21] Morris, J. F., "Lubricated-to-frictional shear thickening scenario in dense suspensions," Phys. Rev. Fluids **3**, 110508 (2018).

[22] Peters, I. R., S. Majumdar, and H. M. Jaeger, "Direct observation of dynamic shear jamming in dense suspensions," Nature **532**, 214–217 (2016).

[23] Singh, A., S. Pednekar, J. Chun, M. M. Denn, and J. F. Morris, "From yielding to shear jamming in a cohesive frictional suspension," Phys. Rev. Lett. **122**, 098004 (2019).

[24] Majumdar, S., R. Krishnaswamy, and A. K. Sood, "Discontinuous shear thickening in confined dilute carbon nanotube suspensions," Proc. Natl. Acad. Sci. U.S.A. **108**, 8996–9001 (2011).

[25] Ramaswamy, M., I. Griniasty, D. B. Liarte, A. Shetty, E. Katifori, E. Del Gado, J. P. Sethna, B. Chakraborty, and I. Cohen, "Universal scaling of shear thickening transitions," J. Rheol. **67**, 1189–1197 (2023).

[26] Anzivino, C., M. Casiulis, T. Zhang, A. S. Moussa, S. Martiniani, and A. Zaccone, "Estimating random close packing in polydisperse and bidisperse hard spheres via an equilibrium model of crowding," J. Chem. Phys. **158**, 044901 (2023).

[27] Seto, R., R. Mari, J. F. Morris, and M. M. Denn, "Discontinuous shear thickening of frictional hard-sphere suspensions," Phys. Rev. Lett. **111**, 218301 (2013).

[28] Goyal, A., N. S. Martys, and E. Del Gado, "Flow induced rigidity percolation in shear thickening suspensions," J. Rheol. **68**, 219–228 (2024).

[29] Maxwell, J. C., "L. *On the calculation of the equilibrium and stiffness of frames*," Lond. Edinb. Dubl. Philos. Mag. J. Sci. **27**, 294–299 (1864).

[30] Seto, R., A. Singh, B. Chakraborty, M. M. Denn, and J. F. Morris, "Shear jamming and fragility in dense suspensions," Granul. Matter **21**, 82 (2019).

[31] O'Hern, C. S., L. E. Silbert, A. J. Liu, and S. R. Nagel, "Jamming at zero temperature and zero applied stress: The epitome of disorder," Phys. Rev. E **68**, 011306 (2003).

[32] Clusel, M., E. I. Corwin, A. O. N. Siemens, and J. Brujić, "A 'granocentric' model for random packing of jammed emulsions," Nature **460**, 611–615 (2009).

[33] Bi, D., J. Zhang, B. Chakraborty, and R. P. Behringer, "Jamming by shear," Nature **480**, 355–358 (2011).

[34] Bertrand, T., R. P. Behringer, B. Chakraborty, C. S. O'Hern, and M. D. Shattuck, "Protocol dependence of the jamming transition," Phys. Rev. E **93**, 012901 (2016).

[35] Mehdipour, I., H. Atahan, N. Neithalath, M. Bauchy, E. Garboczi, and G. Sant, "How clay particulates affect flow cessation and the coiling stability of yield stress-matched cementing suspensions," Soft Matter **16**, 3929–3940 (2020).

[36] Samitsu, S., R. Tamate, and T. Ueki, "Rheological properties of dense particle suspensions of starches: Shear thickening, shear jamming, and shock absorption properties," Langmuir **40**, 26852–26863 (2024).

[37] Pradeep, S., P. E. Arratia, and D. J. Jerolmack, "Origins of complexity in the rheology of soft earth suspensions," Nat. Commun. **15**, 7432 (2024).

[38] Xu, N., and E. S. C. Ching, "Effects of particle-size ratio on jamming of binary mixtures at zero temperature," Soft Matter **6**, 2944–2948 (2010).

[39] Monti, J. M., J. T. Clemmer, I. Srivastava, L. E. Silbert, G. S. Grest, and J. B. Lechman, "Large-scale frictionless jamming with power-law particle size distributions," Phys. Rev. E **106**, 034901 (2022).

[40] Orefice, L., and J. G. Khinast, "Numerical study of bidisperse cohesive particle blends—Bulk properties and critical thresholds," Powder Technol. **428**, 118777 (2023).

[41] Tomas, J., and S. Kleinschmidt, "Improvement of flowability of fine cohesive powders by flow additives," Chem. Eng. Technol. **32**, 1470–1483 (2009).

[42] Jaspers, M., M. T. W. de Wit, S. S. Kulkarni, B. Meir, P. H. M. Janssen, M. M. W. van Haandel, and B. H. J. Dickhoff, "Impact of excipients on batch and continuous powder blending," Powder Technol. **384**, 195–199 (2021).

[43] Amador-Espejo, G. G., A. Suàrez-Berencia, B. Juan, M. E. Bárcenas, and A. J. Trujillo, "Effect of moderate inlet temperatures in ultra-high-pressure homogenization treatments on physicochemical and sensory characteristics of milk," J. Dairy Sci. **97**, 659–671 (2014).

[44] Jeffrey, D., and Y. Onishi, "Calculation of the resistance and mobility functions for two unequal rigid spheres in low-Reynolds-number flow," J. Fluid Mech. **139**, 261–290 (1984).

[45] Jeffrey, D. J., "The calculation of the low Reynolds number resistance functions for two unequal spheres," Phys. Fluids A **4**, 16–29 (1992).

[46] Israelachvili, J. N., *Intermolecular and Surface Forces* (Academic, Waltham, MA, 2011).

[47] Durand, R. V., and C. Franck, "Surprisingly short-ranged interactions in highly charged colloidal suspensions," Phys. Rev. E **61**, 6922–6933 (2000).

[48] Zeng, Y., S. Grandner, C. L. P. Oliveira, A. F. Thünemann, O. Paris, J. S. Pedersen, S. H. L. Klapp, and R. von Klitzing, "Effect of particle size and Debye length on order parameters of colloidal silica suspensions under confinement," Soft Matter **7**, 10899–10909 (2011).

[49] Cundall, P. A., and O. D. L. Strack, "A discrete numerical model for granular assemblies," Geotechnique **29**, 47–65 (1979).

[50] Lees, A. W., and S. F. Edwards, "The computer study of transport processes under extreme conditions," J. Phys. C: Solid State Phys. **5**, 1921 (1972).

[51] Jacobs, D. J., and M. F. Thorpe, "Generic rigidity percolation: The pebble game," Phys. Rev. Lett. **75**, 4051–4054 (1995).

[52] Henkes, S., D. A. Quint, Y. Fily, and J. M. Schwarz, "Rigid cluster decomposition reveals criticality in frictional jamming," Phys. Rev. Lett. **116**, 028301 (2016).

[53] Shapiro, A. P., and R. F. Probstein, "Random packings of spheres and fluidity limits of monodisperse and bidisperse suspensions," Phys. Rev. Lett. **68**, 1422–1425 (1992).

[54] Poslinski, A. J., M. E. Ryan, R. K. Gupta, S. G. Seshadri, and F. J. Frechette, "Rheological behavior of filled polymeric systems. II. The effect of a bimodal size distribution of particulates," J. Rheol. **32**, 751–771 (1988).

[55] Chong, J. S., E. B. Christiansen, and A. D. Baer, "Rheology of concentrated suspensions," J. Appl. Polym. Sci. **15**, 2007–2021 (1971).

[56] Lootens, D., H. Van Damme, and P. Hébraud, "Giant stress fluctuations at the jamming transition," Phys. Rev. Lett. **90**, 178301 (2003).

[57] Liu, J., X. Wu, J. Jiang, Z. Ding, C. Lü, and X. Shi, "A network-based investigation on the strong contact system of granular materials under isotropic and deviatoric stress states," Comput. Geotech. **153**, 105077 (2023).

[58] Lee, C. L., E. Bililign, E. Azéma, and K. E. Daniels, "Particle scale anisotropy controls bulk properties in sheared granular materials," Phys. Rev. Lett. **135**, 108201 (2025).

[59] Singh, S., and G. Buscarnera, "Deciphering how the particle shape modulates the elastic anisotropy of granular media," Comput. Geotech. **176**, 106773 (2024).

[60] Wang, R., W. Cao, and J.-M. Zhang, "Dependency of dilatancy ratio on fabric anisotropy in granular materials," J. Eng. Mech. **145**, 04019076 (2019).

[61] Chigray, I., M. Nabozhenko, G. Abdurakhmanov, and B. Keskin, "A systematic review of the genus *Dila* Fischer von Waldheim, 1844 (= *Caenoblaps* König, 1906, syn.n.) (Coleoptera: Tenebrionidae) from the Caucasus, Turkey and boundary territories of Iran," Insect Syst. Evol. **51**, 753–783 (2020).

[62] Shaebani, M. R., J. Boberski, and D. E. Wolf, "Unilateral interactions in granular packings: A model for the anisotropy modulus," Granul. Matter **14**, 265–270 (2012).

[63] Shaebani, M. R., M. Madadi, S. Luding, and D. E. Wolf, "Influence of polydispersity on micromechanics of granular materials," Phys. Rev. E **85**, 011301 (2012).

[64] De Pascalis, F., and M. Nacucchi, "Relationship between the anisotropy tensor calculated through global and object measurements in

high-resolution x-ray tomography on cellular and composite materials," J. Microsc. **273**, 65–80 (2019).

[65] Lee, C. L., E. Bililign, E. Azéma, and K. E. Daniels, "Loading-dependent microscale measures control bulk properties in granular material: An experimental test of the stress-force-fabric relation," Phys. Rev. E **112**, 035401 (2025).

[66] Boerner, T. J., S. Deems, T. R. Furlani, S. L. Knuth, and J. Towns, Access: Advancing innovation: NSF's advanced cyberinfrastructure coordination ecosystem: Services & support, in *Practice and Experience in Advanced Research Computing 2023: Computing for the Common Good* (Association for Computing Machinery, Portland, OR, 2023), pp. 173–176.

[67] Eigenmann, R., B. E. Bagozzi, A. Jayaraman, W. Totten, and C. H. Wu, "Darwin—A resource for computational and data-intensive research at the University of Delaware and in the Delaware region," Technical Report, Data Science Institute (DSI), University of Delaware, Newark, DE, 2021.